

The effects of irradiation on CrMnFeCoNi high-entropy alloy and its derivatives

Zhouran Zhang, David E.J. Armstrong, Patrick S. Grant*

Department of Materials, University of Oxford, 16 Parks Road, Oxford, OX1 3PH,

United Kingdom

Abstract

High-entropy alloys (HEAs), based on equiatomic or near-equiatomic mixture of usually four or more elements, have attracted considerable attention as there are indications that along with surprising microstructural simplicity of some alloys, they may also offer intriguing combinations of mechanical and other properties. Amongst these properties, there is growing interest in the irradiation response of HEAs and their potential to withstand the neutron bombardment environment of future civil nuclear power plants. One of the first proposed HEAs is face-centred cubic CrMnFeCoNi, also known as the Cantor alloy, and the irradiation response of the Cantor alloy and its sub-systems are the focus of this review. Using irradiation analogues (electrons, heavy ions, and He) to neutron bombardment and considering simulations, advanced microstructural analysis and property measurement, the Cantor alloy and its derivatives are shown to exhibit encouraging irradiation resistance that, in many instances is superior to more traditional dilute alloys of the same elements. The beneficial aspects are high phase stability and resistance to radiation-induced segregation, smaller size but higher number density of dislocation loops, significantly lower extent of swelling and improved resistance to He bubble growth. The future research

directions for irradiation resistant HEAs are also suggested.

Keywords: High-entropy alloys, Cantor alloy, Irradiation response, Radiation resistance, Radiation-induced segregation, Dislocation loops

*Corresponding author.

Email addresses: zhouran.zhang@materials.ox.ac.uk (Zhouran Zhang), david.armstrong@materials.ox.ac.uk (David E.J. Armstrong), patrick.grant@materials.ox.ac.uk (Patrick S. Grant)

1. Introduction

Traditional alloy design concepts are based on one or two elements mixed with a lower concentration of other minority elements to give an overall composition that is optimised for various aspects of performance. This approach has led to, for example, large families of steels [1], aluminum alloys [2, 3], titanium alloys [4] and nickel alloys [5, 6]. Nonetheless, there remains a drive for alloys with superior mechanical and other properties, such as high strength [7], high ductility [8], high fracture toughness [9], creep resistance [10], wear resistance [11], corrosion resistance [12], recyclability [13] and low cost [14]. These incremental improvements are achieved by tailoring the alloy composition and microstructure, for example, by thermo-mechanical processing [15] to reduce grain size [16], to enhance solid-solution effects [17, 18] or to control precipitation hardening [7].

A different approach to alloy design was proposed in 2004 based on equiatomic or near-equiatomic multi-component alloys, typically comprising four or more elements, and has attracted considerable attention [19, 20]. It was hypothesized that the high configurational entropy of equiatomic mixing of multi-elements may promote and stabilise the formation of simple solid solutions rather than a "matrix" predominantly of one or two elements filled with a high volume fraction of usually hard and embrittling intermetallic phases. The equiatomic alloys, proposed simultaneously by Cantor et al. [19] and Yeh et al. [20], have come to be known as high-entropy alloys (HEAs) [20], concentrated solid solution alloys (CSAs) [21] or multi-principal element alloys (MPEAs) [11]. The approach opens up largely unknown "central" regions of al-

loy compositional-phase space. Although the stabilising effect of high configurational entropy of mixing has subsequently been shown not to be a critical feature of the alloys [16, 22], the HEA term remains convenient, and some systems have shown promising mechanical and functional properties [9, 23–25]. In this review, HEA is used as shorthand to describe near-equiatomic, multi-element alloys.

Among the many HEAs studied, the first proposed and one of the foremost systems is the equiatomic, face-centred cubic (fcc) alloy CrMnFeCoNi [19]. This alloy emerged from the work of Cantor et al. [19] and is generally held to be a single phase solid solution, which has become known as the "Cantor alloy" [26]. Considerable efforts have been devoted to understand the alloy mechanical behaviour, corrosion resistance, other intrinsic properties and, more recently, its irradiation response, making it one of the most thoroughly investigated HEA systems [23, 27–29]. The Cantor alloy exhibits some intriguing and attractive mechanical properties [9, 30], particularly an unusual combination of high yield strength (795 MPa), high ultimate tensile strength (1280 MPa), ductility (70%) and fracture toughness ($219 \text{ MPa} \cdot \text{m}^{1/2}$) at cryogenic temperatures [9]. These properties likely result from a relatively low stacking fault energy (approximately $21 \text{ mJ} \cdot \text{m}^{-2}$ at room temperature calculated using quantum mechanical first-principles methods [31] and $18.3\text{--}27.3 \text{ mJ} \cdot \text{m}^{-2}$ measured by X-ray diffraction [32]), a temperature sensitive friction stress, and the onset of widespread deformation nano-twinning at low temperatures [27, 29]. Attention has been growing on the irradiation response of high-entropy alloys, including the Cantor alloy and its sub-systems [21, 33]. Through experiment and computational investigations, the Cantor alloy has been suggested to have

defect energies and other properties that support comparatively good radiation resistance, such as less pronounced void swelling, smaller size of defect clusters and retarded defect growth, migration and evolution, when compared with binary and tertiary sub-systems, and some conventional austenitic steels.

In order to meet rapidly increasing global energy needs, safe, reliable, and economic operation of advanced fission and eventually fusion power plants is generally considered an important element of a lower carbon energy future [34]. One of the key challenges from both scientific and engineering perspectives is how structural materials that are closest to the atomic fission and fusion reactions themselves can retain the required performance under the associated extreme conditions that will involve higher temperatures, higher pressure, a higher irradiation dose and a more corrosive environment for longer periods (up to 80–100 years for key non-replaceable components) than those experienced in current Gen II or Gen III fission reactors [35]. There are a large number of critical requirements for reactor materials including good dimensional stability (thermal stability and low void swelling) [36, 37], favourable mechanical properties (an acceptable combination of tensile strength, ductility, creep resistance, fracture toughness and fatigue resistance) [38, 39], acceptable resistance to radiation damage (less pronounced irradiation-induced defect clusters and thus less irradiation-induced hardening and embrittlement) [40, 41] and high degree of chemical compatibility with the potentially corrosive environment (less stress corrosion cracking with or without irradiation assistance) [37, 42]. In addition, low activation elements are preferred to reduce the radiotoxicity of the most active components during decommissioning. In this sense, the

Cantor alloy may be a less promising candidate for technological implementation. However, HEAs based on less readily activated, but usually more refractory, elements have so far tended to suffer from rapid oxidation, very low toughness and microstructural complexity. Thus the attraction of the Cantor alloy at this early stage of development lies in (i) its microstructural simplicity so that any intrinsic benefits of a multi-component, equiatomic alloying approach to irradiation resistance can be identified, and (ii) that it is relatively easy to process into multi-kg amounts by conventional metallurgical means.

The harsh service conditions and multiple requirements present significant challenges to current structural materials, and in some cases are forecast to constrain reactor design and performance. High-entropy alloys have been suggested to have potential as structural materials for civil nuclear power generation, principally because they offer more opportunities for combining low-activation elements [43], and, in some cases, the possibility of improved mechanical properties [44], improved radiation resistance [23] and related improvement in dimensional stability [45, 46].

There have been many reviews of HEAs [22, 28, 47–49] and the Cantor alloy [27]. Although there have been reviews of irradiation response of single-phase concentrated solution alloys [50–54], given the growing body of work, a review of the irradiation behaviour of the Cantor alloy, its sub-systems, derivatives and related conventional alloys such as austenitic steels is timely. Investigations of the irradiation resistance of other HEAs with no relation to the Cantor alloy system, generally involving more refractory alloying elements, have also started, but are at an earlier - although quickly advancing - stage, and are beyond the scope of this review. Nonetheless, many of the observations and

insights from the Cantor alloy, aided by its microstructural simplicity, will likely apply. This paper reviews state-of-the-art experimental and computational results relating to the irradiation response of the Cantor alloy, its subsystems and derivatives. The irradiation-induced structural damage at room temperature is first discussed in section 2, followed by irradiation-induced damage at elevated temperatures (523-973 K) in section 3. The aspects covered include irradiation-induced solute segregation behaviour, phase stability under irradiation (section 3.1); irradiation-induced defect clusters, such as dislocation lines, loops, voids and bubbles (sections 3.2, 3.3 and 3.4) as well as defect formation, migration and evolution behaviour. Finally, some concluding remarks and comments on future trends are presented.

2. Irradiation-induced structural damage at room temperature

Compared with the more complex microstructural changes experienced at elevated temperatures, defects from irradiation are relatively simple at room temperature [55], and are considered first. Typical induced room temperature changes include the propensity to form and propagate dislocation lines, loops and stacking fault tetrahedra (SFT).

One of the first suggestions that HEAs may have an interesting irradiation response was due to Eagase et al. in 2012 who reported that the structure of a nanocrystalline Zr-Hf-Nb thin film remained stable when irradiated with MeV electrons using an ultra-high voltage electron microscope (UHVEM). At an irradiation dose of up to 10 displacements per atom (dpa) at 298 K, and of up to 50 dpa at 103 K [56], there was an improved radiation resistance compared

with related intermetallic compounds based on similar elements, which amorphized at 0.1-0.5 dpa [57, 58], and Fe-based and Zr-based bulk metallic glasses that crystallized at 1-5 dpa [59–61]. In nanocrystalline CrFeCoNiCu alloy, in-situ TEM (Transmission Electron Microscopy) showed that the fcc solid solution remained as the main constituent phase even under fast MeV electron irradiation of up to 40 dpa at 298 K [62], although there was evidence of minority fcc to bcc (body-centred cubic) phase transitions along with some FeNi L1₀/L1₂ ordering, which were similar to the changes that could also be induced by thermal annealing. Xia et al. and Yang et al. investigated the phase stability and structural damage generated by 3 MeV Au ion irradiation at room temperature and up to 50 dpa in Al_xCrFeCoNi (x = 0.1, 0.75 and 1.5) alloys that formed single fcc, fcc plus ordered bcc (B2) and B2 plus disordered bcc (A2) structures respectively [63, 64]. There was no induced precipitation even at the highest fluence in the single phase system whereas numerous coherent particles were precipitated in the multi-phase microstructure, particularly along phase boundaries [64].

Several studies have investigated the comparative irradiation behaviour of Ni, binary, ternary and quaternary sub-systems of the Cantor alloy. It is worth noting that CoNi, FeNi, CrCoNi, FeCoNi, CrFeCoNi and the Cantor alloys are all fcc. Some of the ternary systems are also becoming known as medium-entropy alloys. Rutherford backscattering spectra and channeling (RBS-C) can be used to investigate crystal quality (e.g. defect density) and determine lattice distortion in crystalline materials; usually, irradiated alloys tend to show higher backscatter yield due to a higher density of interstitial- and/or vacancy-type defect clusters induced by irradiation damage [65]. Fig. 1a and 1b display the

RBS-C scattering yield as a function of depth below the irradiated surface of different Cantor alloy variants at different fluences while Fig. 1c, 1d and 1e show TEM images of the associated defect clusters in Ni, CoNi and FeNi, as well as the defect cluster distribution (Fig. 1f) [21]. With increasing compositional complexity, the induced damage decreased for 3 MeV Au ion and 1.5 MeV Ni ion implantation at various fluences and room temperature (Fig. 1a and 1b). There were nano-sized (2-5 nm) vacancy-type SFT in the region of the highest damage in all irradiated samples, and there were interstitial-type dislocation loops with average sizes of 7.0, 4.3 and 4.4 nm in Ni, CoNi and FeNi respectively. As shown in Fig. 1f, there was a larger fraction of smaller defect clusters in FeNi and CrNi than in Ni. For example, the defect density was 5 times lower than that in Ni. It is suggested that improved radiation resistance in FeNi and CoNi over Ni resulted from intrinsically modified defect energies, dynamics and evolution behaviour in FeNi and CoNi, and these are concepts used to explain irradiation trends in more complex alloys.

[Figure 1 about here.]

Electronic structure calculations using the ab initio Korringa-Kohn-Rostoker coherent-potential-approximation (KKR-CPA) method were used to investigate primary damage formation in displacement cascades. It was shown that a significant reduction in the electron mean free path in CrFeCoNi and FeNi compared with Ni led to more localised electron-electron interactions and heat conduction that effectively delayed the energy dissipation of the electronic subsystems [21]. In addition, molecular dynamics simulation using the Green-Kubo formalism and classical potentials showed that thermal conductivity at room temperature significantly decreased from $88 \text{ W} \cdot \text{m}^{-1} \cdot \text{K}^{-1}$ for Ni to 69.9 W

$\cdot \text{m}^{-1} \cdot \text{K}^{-1}$ for CoNi, $28.0 \text{ W} \cdot \text{m}^{-1} \cdot \text{K}^{-1}$ for FeNi and $12.8 \text{ W} \cdot \text{m}^{-1} \cdot \text{K}^{-1}$ for CrFe-CoNi. The combined effects of reduced thermal conductivity and orders of magnitude reductions in the electron mean free path have been suggested to lead to less efficient heat conduction, and thus a prolonged thermal spike in displacement cascades. Although these may contribute to an improved irradiation response – at least for these closely related alloys – other factors are also likely to be involved, such as the recombination radius.

Fig. 2 shows a comparison of the thermal conductivity of the Cantor alloy and its subsystems, several commercial alloys, and some related BMGs [66–69]. The thermal conductivity of the Cantor alloys and its Cr-containing derivatives (e.g. $\text{Ni}_{80}\text{Cr}_{20}$, CrCoNi, CrFeCoNi, CrMnFeCoNi and CrFeCoNiPd [70]) at room temperature were $10\text{--}15 \text{ W} \cdot \text{m}^{-1} \cdot \text{K}^{-1}$, which was similar to that of commercial alloys (e.g. 304 stainless steel [71], $14.25 \text{ W} \cdot \text{m}^{-1} \cdot \text{K}^{-1}$) but higher than that of BMGs ($4\text{--}8 \text{ W} \cdot \text{m}^{-1} \cdot \text{K}^{-1}$). For binary and tertiary alloys without Cr, thermal conductivities were much higher. For example, FeCoNi exhibited three times higher thermal conductivity than $\text{Ni}_{80}\text{Cr}_{20}$. The specific alloying element rather than simply the number of alloying elements was more significant in determining thermal conductivity, which means increasing compositional complexity when designing alloys does not always lead to reduced thermal conductivity, and thus a more prolonged thermal spike that may help increase vacancy-interstitial recombination rate and reduce defect density.

[Figure 2 about here.]

Similarly, Granberg et al. [65] and Aidhy et al. [72] reported reduced damage in FeNi and CrCoNi compared with Ni by RBS/C. Smaller defect clusters, including $1/3 \langle 111 \rangle$ interstitial-type dislocation loops and vacancy-type SFT,

were observed in FeNi than in Ni [65]. Granberg et al. also conducted MD simulations of Ni, FeNi and CrCoNi to examine radiation collision cascades in the same simulation cell, producing an overall damage of 0.57 dpa, which was comparable with the experimental data. Fig. 3a shows the defect structures in Ni and FeNi and Fig. 3b shows the defect distribution grouped by cluster size and cluster diameter. There was a larger fraction of small clusters in FeNi and CrCoNi compared with Ni, which agreed with the TEM observations of Lu et al. [73] Apart from the effect of a reduction of thermal conductivity and electron mean free path, defects were suggested to migrate more slowly in FeNi than in Ni due to modified defect migration energies and a transition from 1D dislocation motion in Ni to 3D motion in FeNi [73]. Thus, the production and migration of defects were limited to a more confined, local volume in FeNi, leading to a higher rate of recombination. This finding emphasises that the factors governing the recombination rate between interstitials and vacancies are complex, even in apparently simple alloys, making simple and robust criteria for irradiation resistance difficult to identify. Transition of dislocation motion from 1D in Ni to 3D in FeNi will be discussed in detail in Section 3.2 while further consideration of the defect migration energies of the derivatives of the Cantor alloy are given below.

[Figure 3 about here.]

Fig. 4 shows the calculated energy barriers to the migration of interstitials and vacancies in FeNi, CrCoNi and CrFeCoNi respectively, with dashed lines as the energy barriers for Ni ($E_m^v = 1.05$ eV and $E_m^v = 0.15$ eV). As shown in Fig. 4, a significant feature is that the point defect formation and migration energies of the derivatives of the Cantor alloy present as a statistical distribution instead

of a single value [74–76]. The migration barrier of interstitials was in general smaller than that of vacancies in FeNi, CrCoNi and CrFeCoNi, which was consistent with most metals where interstitials are highly mobile whereas vacancies are relatively immobile. Overall, the interstitials in the alloys had higher migration barriers and lower diffusion coefficients [77, 78] than in Ni. In contrast, the energy barrier to vacancy migration in FeNi, CrCoNi, and CrFeCoNi were either slightly smaller or similar to that of Ni, with migration facilitated by Fe in FeNi, and Cr in both CrCoNi and CrFeCoNi [23, 75–77].

Another feature of the migration energies for point defects in the derivatives of the Cantor alloy is the prominent overlapping energy region for vacancies and interstitials. Due to generally slower interstitial migration and relatively fast vacancy migration, the recombination rate and frequency of defect annihilation will likely be promoted in FeNi, CrCoNi and CrFeCoNi, agreeing well with the general trend of experimental results.

[Figure 4 about here.]

To investigate the effect of Fe concentration alone on irradiation resistance, a series of $\text{Fe}_{1-x}\text{Ni}_x$ ($0 < x < 60$ at.%) alloys were irradiated with Ni ions over a wide range of fluences from 3×10^{13} to $3 \times 10^{16} \text{ cm}^{-2}$ [79]. At low fluences, RBS-C results showed reduced damage accumulation with increasing Fe concentration. In the high fluence regime ($5 \times 10^{15} \text{ cm}^{-2}$ - $3 \times 10^{16} \text{ cm}^{-2}$), defect size decreased dramatically with increasing Fe concentration while the density of defect clusters was smaller in Ni than that in $\text{Ni}_x\text{Fe}_{1-x}$. Fig. 5a, 5b and 5c display the TEM images of Ni, $\text{Ni}_{80}\text{Fe}_{20}$ and FeNi irradiated at a fluence of $5 \times 10^{15} \text{ cm}^{-2}$. Large dislocation loops ($>30 \text{ nm}$) were frequently ob-

served in Ni whereas in the binary alloys, especially in FeNi, most of the defects were “black dot defects” identified to be either small interstitial loops of a few nm or vacancy type SFT. Fig. 5d shows the defect size distribution in Ni, Ni₈₀Fe₂₀ and FeNi alloys after irradiation at a fluence of $5 \times 10^{15} \text{ cm}^{-2}$ and at a depth of 350 nm, corresponding to the region with a peak dose of $\sim 6.5 \text{ dpa}$. The average size of defects in Ni, Ni₈₀Fe₂₀ and FeNi were approximately 9, 4, and 3 nm with a defect density of 0.4, 1.2, and $1.9 \times 10^{23} \text{ m}^{-3}$ respectively. MD simulations also showed that with increasing Fe concentration, the number of surviving displaced atoms reduced [79]. It should be noted that atom probe tomography (APT) results showed no clear evidence of any irradiation-induced compositional segregation and precipitation and there was a near homogeneous distribution of elements, even at higher fluences of up to $3 \times 10^{16} \text{ cm}^{-2}$. These findings are consistent with studies discussed above suggesting that binary and tertiary sub-systems of the Cantor alloy retain relatively high levels of compositional homogeneity after room temperature irradiation.

[Figure 5 about here.]

In summary, the irradiation behavior at room temperature of the Cantor alloy and its derivatives including Ni, CoNi, FeNi, CrCoNi, CrFeCoNi, CrFeCoNiCu and Al_xCrFeCoNi ($x = 0.1, 0.75$ and 1.5) has been investigated. Other than minor phase changes and ordering in nanocrystalline CrFeCoNiCu, and precipitation in dual-phase Al_xCrFeCoNi ($x = 0.75$ and 1.5), all other alloys retained the starting phase distribution. There were small defect clusters, including $1/3 \langle 111 \rangle$ interstitial-type dislocation loops and vacancy-type SFT in all the alloys. TEM studies focused on Ni and binary alloys, and have suggested improved radiation damage in FeNi and CoNi when compared with Ni. Ab initio

modeling and MD simulations suggested that increased irradiation resistance is due to a synergistic effect of higher interstitial-vacancy recombination rate (prolonged thermal spike) and retarded defect growth (modified defect dynamics).

3. Irradiation-induced structural damage at elevated temperatures (523-973 K)

The structural materials used in current nuclear reactors are exposed to energetic particle irradiation at elevated temperature, and structural materials in future nuclear reactors are forecast to be exposed to even higher irradiation doses and temperatures [37, 39, 42]. During irradiation damage at elevated temperature, the spatial redistribution of solute and impurity elements by diffusion is enhanced, which may lead to localised enrichment or depletion of alloying elements at dislocation loops, voids, grain boundaries and phase boundaries, and more stable phases (lower free energy than the starting phases as these phases become more defective) may form [80–82]. Together with irradiation induced dislocation lines and dislocation loops, elevated temperature can accelerate changes in macroscopic properties, leading to pronounced hardening and embrittlement [83, 84]. The formation and growth of voids and gas bubbles are also well-known for their negative influence on material performance in radiation environments at elevated temperature [85–87].

In this section, segregation and phase stability against irradiation at elevated temperatures is discussed, followed by detailed consideration of irradiation-induced dislocation lines, loops, voids and bubbles. The type of loops, the fractions of partial and perfect loops, the loop density and average loop size in the

Cantor alloy and its derivatives under electron and heavy ion irradiation are considered. Void formation, volume swelling and gas bubbles formation behaviour are summarised, as well as their typical distribution of loops and voids in different alloys. Intrinsic mass and thermal transport properties, the formation and migration energies of point defects and their impact on the growth and evolution of defect and defect clusters, are also considered.

3.1. Irradiation-induced segregation and phase stability under irradiation

Radiation-induced segregation (RIS) is caused by the interaction between the induced flux of vacancy and interstitial point defects and the flux of solutes to point defect sinks [88], such as grain boundaries, dislocations and voids. Enrichment or depletion of solute can lead directly to precipitation if local solute concentrations exceed the solubility limit. RIS can result in the degradation of macroscopic properties, for instance, it has been known for decades that radiation-induced depletion of Cr at grain boundaries contributes to irradiation-assisted stress corrosion cracking (IASCC) in austenitic stainless steels [89, 90].

Similarly to the phase stability under irradiation at room temperature discussed in section 2, in nanocrystalline (with grain sizes of ~ 10 nm) CrFeCoNiCu, the fcc solid solution remained the main phase under fast MeV electron irradiation of up to 40 dpa at 773 K [62], although there was some minor fraction of transformed bcc and B2-type FeCo and FeNi L_{10}/L_{12} ordering. The phase stability of CrFeCoNi, CrMnFeCoNi and CrFeCoNiPd against 1250 keV electrons of up to 1 dpa at 673 K has been reported [91]. Phase separation and ordering again took place in CrMnFeCoNi and CrFeCoNiPd but there was no

detectable phase separation/decomposition in CrFeCoNi alloy. Fig. 6 shows $\langle 001 \rangle$ -oriented spinodal decomposition (Fig. 6a) and L_{10} (NiMn)-type ordering (Fig. 6b) in electron-irradiated CrMnFeCoNi. In contrast, no phase separation/decomposition was observed in either CrMnFeCoNi or CrFeCoNiPd alloys, in this case irradiated with 3 MeV Ni ions at 653, 773 and 853 K to a fluence of $5 \times 10^{16} \text{ cm}^{-2}$ [92, 93]. When compared with ion irradiation, relatively low primary knock-on atom energies were produced from electron irradiation, which likely contributed to different microscopic changes in nominally the same alloy. The role of far from equilibrium highly defective states generated by ion irradiation on the thermodynamic balance between enthalpy and entropy effect on phase stability must also be considered.

[Figure 6 about here.]

It is worth pointing out that although the Cantor alloy retained a simple fcc solid solution even after long annealing up to 500 days [94] at relatively high temperatures (over 1073 K), it decomposed into multiple phases at intermediate (773-973 K) annealing temperatures after 500 days [95–96]. Fig. 7 shows Scanning Transmission Electron Microscopy (STEM) images superimposed with Energy Dispersive X-ray Analysis (EDX) maps and corresponding SAED patterns of the Cantor alloy annealed at 773 K for 500 days. The alloy decomposed into three phases, i.e. L_{10} -type NiMn, bcc Cr-rich solid solution and B2-type FeCo [94]. There was L_{10} (NiMn)-type ordering both after annealing and electron irradiation, which may be attributed to more negative enthalpy of mixing for L_{10} -type NiMn ordering [62]. It is unclear whether there was radiation-induced precipitation and decomposition, distinct from thermal effects, in the Cantor alloy, and if so, how ongoing irradiation resistance was affected.

[Figure 7 about here.]

Note that the Cantor alloy is not thermodynamically stable solely as a solid solution at the intermediate temperatures (773-973 K), which is likely the service temperature for structural materials in advanced nuclear reactors, such as lead-cooled fast reactors (LFR), sodium-cooled fast reactors (SFR) and super critical water-cooled reactors (SCWR) with core outlet temperatures of 823-1273K, 823 K and 628-993 K respectively [35, 39].

Barr et al. explored the RIS behaviour of the Cantor alloy under 3 MeV Ni ion irradiation at 773 K and a fluence up to $3 \times 10^{15} \text{ cm}^{-2}$ [97]. Fig. 8a shows representative irradiation-induced segregation profiles at a randomly selected high angle grain boundary (HAGB) at 2 dpa, while Fig. 8b compares the compositional change along GBs to regions away from GBs for the Cantor alloy and conventional fcc alloys (304 high and commercial purity [80], model Ni-Cr alloys [81, 98], and model Fe-Ni-Cr alloys [81]). There was a substantial depletion of Mn and enrichment of Co and Ni along HAGBs at both 2 and 3 dpa, which followed similar trends to the RIS behaviour in conventional Fe-Ni-Cr alloys. Self-diffusion radiotracer diffusion coefficient measurements at high temperature [99] showed that the fastest and slowest diffuser were Mn and Co respectively, leading to a corresponding depletion of Mn and enrichment of Co based on the vacancy dominated inverse Kirkendall mechanism [82]. The magnitude of segregation was similar for the Cantor alloy and for conventional Fe-Ni-Cr alloys under similar irradiation conditions.

[Figure 8 about here.]

Kumar et al. [100] studied the irradiation behaviour of a Co-free $\text{Cr}_{18}\text{Mn}_{27}\text{Fe}_{27}\text{Ni}_{28}$ single-phase alloy irradiated with 3 or 5.8 MeV Ni ions at

temperatures ranging from room temperature to 973 K, and up to 10 dpa. There were no phase changes according to X-ray diffraction but there was enrichment of Ni and depletion of all other three elements at GBs, with concentration variations between matrix and GB in the trend order $\text{Ni} > \text{Fe} > \text{Cr} > \text{Mn}$. When compared with more conventional $\text{FeCr}_{20}\text{Ni}_{24}$, the solute segregation in $\text{Cr}_{18}\text{Mn}_{27}\text{Fe}_{27}\text{Ni}_{28}$ was significantly reduced.

Chemical segregation along defect clusters can also occur. For example, Yang et al. compared the structural damage and chemical segregation in $\text{Al}_{0.1}\text{CrFeCoNi}$ irradiated at different temperatures ranging from 523 K to 823 K. TEM and APT showed there were no significant phase changes at high temperature, but there was enrichment of Ni and Co as well as depletion of Fe and Cr at defect clusters (largely dislocation loops). The concentrations of Co, Cr, Fe, and Ni varied by 30–50% from the matrix to the dislocation loops, with Co and Fe showing slightly more segregation than Ni and Cr [101]. With increasing temperature, the magnitude of segregation increased.

RIS behaviour at defect clusters in FeNi, FeCoNi, CrFeCoNi and CrMnFeCoNi was also investigated using electron energy loss spectroscopy [93]. Fig. 9 shows a STEM-BF image of an interstitial-type dislocation loop in irradiated Cantor alloy and corresponding compositional line scan profiles across dislocation loops in the four alloys. Frank dislocation loops were enriched with Ni and Co, and depleted in Cr and Fe in FeNi, FeCoNi, CrFeCoNi, whereas there was no obvious segregation in CrMnFeCoNi, suggesting significantly lower RIS in the Cantor alloy.

[Figure 9 about here.]

RIS to defects will depend upon the propensity to form such defects and

the equilibrium concentration of vacancies and interstitials at a given temperature will be determined by the associated defect formation energies. Using ab initio calculations and empirical potentials, Zhao et al. calculated the formation energy of interstitials and vacancies in FeNi, CrCoNi and CrFeCoNi, which are shown in Fig. 10, with the formation energy for Ni marked by a black dashed line. Similar to defect migration energies, the defect formation energies again present as a distribution, with an overlap of interstitial and vacancy formation energies. Generally, the formation energy of preferred [100] interstitial dumbbells (E_f^i) in alloys was lower than that in Ni (3.96 eV [76] and 4.27 eV [75]) while the formation energy of vacancies (E_f^v) was higher than that in Ni ($E_f^v \approx 1.45$ eV [75, 76]).

Considering various possible dumbbell interstitials in HEAs, preferable diffusion channels due to lower formation energies of certain types of dumbbells were observed, which can be expected to affect the RIS behaviour along defect clusters. For example, in FeNi, the lower formation energy of a [100] Ni–Ni dumbbell than a [100] Fe–Fe dumbbell suggested that interstitial defects will preferentially diffuse in Ni and not Fe [75]. In contrast, Co-containing (e.g. Co–Co, Co–Fe and Co–Cr) dumbbells in CrFeCoNi had, in general, a lower formation energy than Ni–Ni dumbbells, leading to preferable binding of Co interstitials [76]. These observations agreed well with interstitial-dominated RIS behaviour along interstitial loops for Ni/Co enrichment and Fe depletion in FeNi and CrFeCoNi discussed above.

[Figure 10 about here.]

With regard to vacancy formation energy, Ni vacancies prefer a Ni-rich local environment and Fe vacancies prefer a Fe-rich environment in FeNi because the formation energy of Ni vacancies tends to decrease whereas the formation energy of Fe vacancies tends to increase as there is an increase in the fraction of nearest Ni neighbours. In both CrCoNi and CrFeCoNi, Cr vacancies had the highest formation energy among the three vacancy types. Vacancies will likely favour a Ni-rich as well as Co/Cr-depleted environment because more Ni atoms in the first-nearest-neighbor shell surrounding vacancies leads to a lower vacancy formation energy [75] while more Co and Cr atoms in the first-nearest-neighbour shell leads to an increase in vacancy formation energy. It is then expected that Ni will enrich at vacancy-type defect clusters in FeNi, CrCoNi and CrFeCoNi. This trend has also been observed in a model FeCr₂₀Ni₁₀ austenitic steel due to strong binding interactions between Ni and vacancies [102].

It is worth noting that the calculated formation energies showed sensitivity to the chosen size of the finite supercell, as well as the assumed chemical potentials, in the ab initio calculations. Calculated formation energies were likely to be overestimated if small supercells were used due to a periodic image effect [75] and led to a wider spread of formation energies compared with calculations based on larger supercells [76, 103, 104]. A detailed comparison between ab initio calculations based on directly computed chemical potentials and calculations based on available embedded atom method (EAM) potentials suggested that the EAM method failed to capture the strongly composition-dependent formation energy behaviour of all the alloys.

Overall, the Cantor alloy and its derivatives exhibit good phase stability

under heavy ion irradiation. Radiation-induced segregation to grain boundaries and defect clusters is similar or lower in extent in the Cantor alloy and its derivatives compared with more traditional dilute alloys, with depletion of Mn/Fe and enrichment of Ni/Co, principally due to chemically-biased interstitial diffusion.

3.2. Irradiation-induced dislocation lines and loops

Frenkel pair (vacancy and interstitial pair) can form during irradiation-induced collision cascades, where a portion of such pairs survive and then contribute to the overall defect and defect cluster population. Simultaneously, induced dislocation loops may disappear by annihilation with vacancies or encountering sinks but may also grow by the absorption/influx of interstitials. Dislocation lines and loops are known to have significant impact on macroscopic properties, for example causing hardening and embrittlement [105, 106].

He et al. showed that there were interstitial-type, either elliptical Frank loops or polygonal (mostly rhombus) perfect loops in a CrFeCoNi under 400, 500 and 1250 kV in situ electron irradiation at 673 K and up to 1 dpa [107]. Fig. 11a and b show the growth behaviour of a Frank loop and a perfect loop after 2 min, 15 min and 30 min of irradiation. Fig. 11c shows the major axis length of loops as a function of damage level.

Loops in CrFeCoNi exhibited non-linear power law growth that was more than 40 times slower than the near-linear defect growth behaviour of Ni, which likely resulted from the reduced mobility of defect clusters either due to enhanced solute pinning [108] or the differences in migration energies, as discussed in Section 2 [72]. The recombination of vacancies and interstitials was

consequently promoted and their agglomeration into dislocation loops dramatically suppressed [107]. All dislocation loops were identified as interstitial-type and the elliptical Frank loops as $1/3 \langle 111 \rangle$ type, and the rhombus perfect loops as $1/2 \langle 110 \rangle$ type [91]. The majority of loops nucleated within 1 min of irradiation, and the loop density saturated within 5 min. Two forms of loops were produced simultaneously, in a number ratio close to 3 (faulted): 1 (perfect), and no faulted loop was observed to transform to a perfect loop, or vice versa.

[Figure 11 about here.]

CrMnFeCoNi and CrFeCoNiPd were also irradiated under the same conditions as a CrFeCoNi (1250 kV electrons, 673 K and 1 dpa). The density of loops was much lower while the loop sizes were larger in the quinary alloys compared with CrFeCoNi [91, 107]. Although there were both type of loops in CrMnFeCoNi and CrFeCoNiPd, the fraction of perfect loops was lower in the quinary alloys. He et al. suggested this may arise due to the reduced stacking fault energy of the quinary alloys compared with CrFeCoNi [91], although other work has suggested that the SFE of CrFeCoNiPd may be the highest among these alloys [109, 110].

As pointed out in section 3.1, it may be problematic to extrapolate the low primary knock-on atom energy produced by relatively convenient electron irradiation to the more energetic displacement cascade conditions under fast neutron radiation, where the latter is generally the preferred simulation to approximate the irradiation environment in a power plant [111, 112].

Ni, FeNi, CoNi, FeCoNi, CrFeCoNi and CrMnFeCoNi were irradiated with 1.5 or 3 MeV Ni ions at 773 K [23] and both voids and dislocation loops were

readily observed. Fig. 12 shows the distribution of dislocations, dislocation loops and voids in Ni and the five alloys. There were dislocation networks in irradiated Ni, FeNi, CoNi and CrFeCoNi and long dislocation lines and larger dislocation loops formed at greater sub-surface depth than voids in Ni and CoNi. Dislocation loops formed near the sample surface, extending to a depth of 600 nm, followed by a region containing a comparatively low density of small voids in FeNi and CrFeCoNi. Similar results in terms of the nature and distribution of defect clusters were also reported by Yang et al. [113].

[Figure 12 about here.]

Although the interstitial clusters in Ni and FeNi generally migrated one-dimensionally along the $\langle 110 \rangle$ direction, they changed directions randomly in FeNi, forming a number of 1D $\langle 110 \rangle$ segments (length of the $\langle 110 \rangle$ segments within 20 ns was about 1 nm for FeNi at 1200 K). The shorter a 1D migration segment, the more frequently interstitial clusters may change direction. In this case, interstitials were shown through MD simulations to move in 1D in Ni relatively long distances without encountering and annihilating with vacancies. Small interstitial clusters in Ni moved quickly from the high dpa damage region to the surface or to deeper regions, leaving a high concentration of vacancies susceptible to detrimental void formation. In contrast, interstitials migrated randomly in 3D in FeNi, producing a high proportion of annihilation events with neighboring mono-vacancies and vacancy clusters, leading to a smaller concentration of residual voids.

In addition, the energy barrier to vacancy cluster migration is calculated to be smaller than that of a single vacancy in FeNi (di-vacancy migration energy ≈ 0.515 eV). Di- and tri-vacancy clusters had migration energies similar to

that of a single interstitial, so that interstitials and vacancies can migrate simultaneously, encouraging a higher recombination rate and lower concentration of surviving defects in FeNi than in CoNi or Ni [23, 73].

Similarly, dislocation loop density and the average size of loops have been reported for FeNi, FeCoNi, CrFeCoNi and CrMnFeCoNi irradiated with 3 MeV Ni ions at 773 K and up to 38 ± 5 dpa [93]. Fig. 13 displays two-beam condition BF TEM images from these four alloys, showing both perfect loops with $1/2 \langle 110 \rangle$ and Frank loops with $1/3 \langle 111 \rangle$, similar to those obtained under high energy electron irradiation [91, 101].

[Figure 13 about here.]

Fig. 14 shows the loop density, loop size distribution, average diameter of loops and fraction of faulted loops in the above four alloys. The trend in loop density was $\text{CrMnFeCoNi} > \text{CrFeCoNi} = \text{FeCoNi} > \text{FeNi}$, where the loop density was approximately one magnitude higher in CrMnFeCoNi and two times higher in CrFeCoNi and FeCoNi than in FeNi. In contrast, the average diameter of loops in FeNi, FeCoNi, CrFeCoNi and CrMnFeCoNi was 76 nm, 42 nm, 51 nm and 24 nm respectively, and large loops with a diameter of over 150 nm were only present in FeNi. There was a higher fraction of faulted loops in more compositionally complex alloys (52%, 34%, 17% and 8% respectively in CrMnFeCoNi, CrFeCoNi, FeCoNi and FeNi), which was attributed to a reduction in transformation of faulted to perfect loops due to a lower stacking fault energy [93, 109].

[Figure 14 about here.]

There are some discrepancies in the literature relating to characterisation

of dislocation loops and their evolution. For example, in some reports, the density of loops in CrMnFeCoNi and CrFeCoNiPd was lower, and the loop sizes larger, when compared with CrFeCoNi after high energy electron irradiation [91, 107] and both perfect loops with $b = 1/2 \langle 110 \rangle$ and Frank loops with $b = 1/3 \langle 111 \rangle$ formed simultaneously without the need for a transition from faulted loops to perfect loops [91, 107]. Elsewhere, it has been reported that the density of loops in CrMnFeCoNi was approximately 5 times higher than that of CrFeCoNi while the average diameter of loops was only one half that of CrFeCoNi after heavy ion irradiation [23, 93]. Moreover, the higher fraction of faulted loops in ion irradiated CrMnFeCoNi was attributed to a lower tendency for the transformation of faulted loops to perfect loops, apparently at odds with the previous finding that no such transition was needed for perfect loop formation under in-situ electron irradiation. It should be noted that there are significant challenges in comparison of findings from different experiments due to the challenges in keeping consistent materials, comparable irradiation conditions and imaging techniques, and that quantification is sensitive to sample preparation, surface contamination and imaging conditions.

To investigate further whether dislocation loop transitions occur (e.g. faulted = perfect dislocation loops), in-situ TEM has been used to probe the defect evolution in Ni, FeNi, CoNi, CrCoNi, CrFeCoNi, CrMnFeCoNi and CrFeCoNiPd irradiated with 1 MeV Kr ions at 773 K and from 0.1 to 2 dpa [114]. Loops transformed from faulted Frank loops to perfect loops in FeNi and CrFeCoNi, but at different ion doses, the explicit reasons for which are hard to identify. Fig. 15 shows the defect density and defect average size for

the different alloys. In general, the density of loops decreased in the trend order Ni, CoNi, FeNi, CrCoNi, CrFeCoNi, CrMnFeCoNi and CrFeCoNiPd, while the mean defect size increased with increasing ion dose in the trend order Ni, CoNi, CrCoNi, FeNi, CrFeCoNi, CrMnFeCoNi, of up to 2 dpa. This contradicts other studies in nominally the same alloys albeit under different ion species and doses [91, 93, 101].

[Figure 15 about here.]

In a $\text{Cr}_{18}\text{Mn}_{27}\text{Fe}_{27}\text{Ni}_{28}$ alloy irradiated with 3 or 5.8 MeV Ni ions at temperatures ranging from room temperature to 973 K up to 10 dpa [100], there was a relatively high density of small dislocation loops at all temperatures. The loop density was nearly independent of dose at low temperature whereas the loop density monotonically decreased and loop sizes monotonically increased with increasing temperature. Fig. 16 shows the loop density as a function of irradiation temperature in $\text{Cr}_{18}\text{Mn}_{27}\text{Fe}_{27}\text{Ni}_{28}$ and in conventional austenitic alloys irradiated under similar conditions [115–128]. The overall loop densities were significantly higher in irradiated $\text{Cr}_{18}\text{Mn}_{27}\text{Fe}_{27}\text{Ni}_{28}$, for instance, the loop density in $\text{Cr}_{18}\text{Mn}_{27}\text{Fe}_{27}\text{Ni}_{28}$ was nearly 50 times greater than that of $\text{FeCr}_{15}\text{Ni}_{20}$ when irradiated at 948 K and up to 30 dpa (Note that dislocation lines and tangled dislocations were not included in the counting) [118]. The Cantor alloy also exhibited an order of magnitude higher loop density than its ternary sub-systems, but also much smaller average diameter of loops due to the slower defect growth dynamics described earlier.

[Figure 16 about here.]

Fig. 17 shows dislocation loops, network dislocations and SFT in a

Al_{0.1}CrFeCoNi irradiated by 3 MeV Au ions at different temperatures from 523 K to 923 K. In this case, defect density decreased but defect size increased with increasing irradiation temperature [101]. The defect clusters were suggested to transform from faulted loops and small defect clusters to perfect loops, SFT and long dislocation lines with increasing temperature.

[Figure 17 about here.]

Al_{0.3}CrFeCoNi, CrMnFeCoNi and 316H stainless steel were irradiated using in-situ 1 MeV Kr ions at 573 K and up to 1 dpa [129]. Fig. 18 shows TEM images of dislocation loops in these alloys as well as the density and average size of loops as a function of dose. There was a high density of faulted Frank loops with $b = 1/3 \langle 111 \rangle$ lying on $\{111\}$ planes in all three alloys; loops appeared at 0.01 dpa and the density was saturated at 0.1 dpa. Nanoindentation showed that the degree of irradiation hardening was also comparable, and agreed with the findings of Kumar et al. [100] from an ex-situ, low-temperature and low-dose irradiation study of Cr₁₈Mn₂₇Fe₂₇Ni₂₈. At a lower temperature (573K), it was contended that any intrinsic features of HEAs had a negligible effect on irradiation-induced microscopic hardness.

[Figure 18 about here.]

Overall, there are interstitial-type, either elliptical Frank loops $1/3 \langle 111 \rangle$ or rhombus perfect loops $1/2 \langle 110 \rangle$, in the Cantor alloy and its derivatives under electron and heavy ion irradiations at elevated temperature. Although there are some discrepancies in terms of the size and density of loops, as well as loop evolution of faulted to perfect loops, possibly due to different primary knock-on energy and errors introduced from counting procedures, the Cantor alloy shows a higher number density but much smaller size of dislocation loops

compared with its binary and tertiary sub-systems, and conventional fcc alloys. Complex dislocation networks and long dislocation lines form in less compositionally complex alloys, but not in the Cantor alloy, which could suggest an extended incubation period and retarded defect growth kinetics.

3.3. Void swelling

At temperatures between $0.3 T_M$ and $0.6 T_M$ (T_M = absolute melting temperature; $T_M = 1553$ K for the Cantor alloy), the agglomeration of irradiation-induced vacancies and the growth of voids can cause pronounced volume swelling, degrade material performance, and thus have a significant deleterious impact on allowable lifetime and reactor operations [39, 119, 126, 130]. Earlier studies have shown that void formation is expected in conventional Fe-Cr-Ni alloys for ion irradiation doses above 1-10 dpa at 623 K to 923 K [131], and susceptibility to swelling in Fe-Cr-Ni alloys can be modified by varying the Ni and Cr concentration. For instance, higher Cr concentrations lead to a lower vacancy diffusion coefficient and supersaturated vacancies can cluster into voids within a very short time [132].

Fig. 19 shows the extent of swelling measured using an optical profilometer and corresponding cross-sectional TEM images of voids in Ni, CoNi, FeNi, CrCoNi, FeCoNi, CrFeCoNi and CrMnFeCoNi irradiated with 3 MeV Ni ions to $5 \times 10^{16} \text{ cm}^{-2}$ (peak dose 53 dpa) at 773 K [133, 135]. All six alloys exhibited significantly lower void swelling than Ni. According to optical profilometry, the void swelling of Ni was 6.7% whereas CrMnFeCoNi and FeCoNi showed the lowest void swelling of <0.2%, and was approximately similar for the FeNi. However, according to TEM characterisation [133, 135], the average size of

voids in the FeNi was much larger (44.9 nm [135]) than in the Cantor alloy (14.1 nm [135]), but the number density of these smaller voids was approximately five times higher in the Cantor alloy [135]. The lower number density of large vacancy clusters in the Cantor alloy, which have greater potential to undermine to long-term properties, may be due to a relatively high interstitial-vacancy recombination rate, and/or that larger vacancy clusters were relatively immobile.

Fe additions were more effective in reducing void swelling than Co, and the void swelling was not simply related to the extent of alloying only. For example, FeNi showed lower void swelling than CrCoNi and CoNi, and FeCoNi exhibited similar void swelling to CrMnFeCoNi, which suggests that the intrinsic irradiation resistance of alloying elements should be considered in searching for HEAs with high irradiation tolerance [133], although comparable data for all elements of interest are not yet easily available.

[Figure 19 about here.]

Fig. 20 shows cross-sectional TEM images of CoNi, FeNi, FeCoNi, CrFeCoNi and CrMnFeCoNi irradiated with 1.5 MeV Ni ions ($3 \times 10^{15} \text{ cm}^{-2}$) and/or 3 MeV Ni ions ($5 \times 10^{16} \text{ cm}^{-2}$) at 773 K [23]. The void swelling of Ni was 1.8% while CrMnFeCoNi had a swelling of 0.02%. The overall void swelling resistance can be ranked in the order $\text{Ni} < \text{CoNi} < \text{FeNi} \leq \text{CrFeCoNi} < \text{FeCoNi} \leq \text{CrMnFeCoNi}$. As discussed earlier, the migration energy barrier for vacancy cluster in FeNi was lower than that of a single vacancy, which can result in a higher recombination rate of interstitials and vacancies and thus a lower concentration of surviving defects [23, 73]. Furthermore, with increasing size of clusters, MD simulations showed that the diffusion coefficient of vacancy clusters

decreased rapidly and clusters containing more than 7-13 vacancies migrated much slower in NiFe, Ni₈₀Fe₂₀, Ni₈₀Cr₂₀ and Ni₄₀Fe₄₀Cr₂₀ than in Ni [46]. This finding is consistent with the observed trend in void swelling behaviour in Ni, FeNi and CrFeCoNi.

[Figure 20 about here.]

No detectable void formation at any of the ion irradiation conditions studied was observed in Cr₁₈Mn₂₇Fe₂₇Ni₂₈ irradiated with 3 or 5.8 MeV Ni ions at temperatures from room temperature to 973 K and up to 10 dpa [100]. Fig. 21 presents a comparison of the swelling behaviour of the Cantor alloy, its derivatives, and conventional steels (e.g. 316SS, FeCr₁₅Ni₁₆) under similar irradiation conditions [115,116,134,135], in terms of void average size (nm, square marks) and void number density (10²⁰ m⁻³, circles). The Cantor alloy and CrFeCoNi exhibited a nearly order of magnitude lower overall swelling (0.072% and 0.016% at 773 K and 60 dpa respectively) than conventional alloys (0.46% for 316SS at 773 K and 50 dpa [115] and 1.23% for FeCr₁₅Ni₁₆ at 773 K and 16.4 dpa [116]) under similar or even harsher conditions. The lower swelling was principally due to their smaller average void diameters.

[Figure 21 about here.]

To assess the dependence of void swelling on irradiation temperature, CrCoNi, CrMnFeCoNi and CrFeCoNiPd were irradiated with 3 MeV Ni ions at 693 K, 773 K and 853 K and at a fluence of $5 \times 10^{16} \text{ cm}^{-2}$ [92, 136]. An additional irradiation temperature of 923 K (0.61 T_M) was also applied to the Cantor alloy, but no voids were observed. Fig. 21 shows the cross-sectional TEM

images of three alloys irradiated at different temperatures. In CrCoNi, at 693 K, void swelling was suppressed in the high Ni ion concentration region (~ 1000 nm below the surface), as shown in Fig. 21a. The greatest swelling was in CrCoNi (0.24%) while CrMnFeCoNi and CrFeCoNiPd had only 0.02% and 0.003% swelling respectively. The average void size in CrCoNi was nearly 4 times and 6 times higher than CrMnFeCoNi and CrFeCoNiPd, while the void number density in CrCoNi was more than one magnitude higher than the two quinary alloys.

At 773 K and 853 K, the migration rate of interstitials in CrCoNi increased so that they escaped towards the surface or into deeper regions without significant recombination with vacancies and there were no zones denuded of voids. In contrast, there was only a comparatively small fraction, of smaller voids, in CrMnFeCoNi beyond 1000 nm depth from the surface at all temperatures, as shown in Fig. 21b and 21c. There were voids in all regions of CrFeCoNiPd at all temperatures. Density-functional theory (DFT) modeling of $\text{Ni}_{80}\text{X}_{20}$ (X=Cr, Mn, Fe, Co, Ni and Pd) binary alloys [74] may help to shed light on the different distribution of voids in these three alloys. The vacancy formation energy of $\text{Ni}_{80}\text{Pd}_{20}$ was calculated to be lower than that of the other four binary alloys, which likely led to a more widespread spatial distribution of voids seen in experiments. Void number density and average void size were also both significantly higher in CrCoNi than in the quinary alloys. At 773 K, although the void number density in CrMnFeCoNi was nearly 4 times higher than in CrFeCoNiPd, the average void size was ~ 2 times smaller, contributing to slightly less void swelling in CrMnFeCoNi (0.07%). At 853 K, 0.37% swelling in CrMnFe-

CoNi was slightly higher than 0.3% in CrFeCoNiPd due to an increased average void size (92 nm vs. 67 nm), despite a lower void number density.

[Figure 22 about here.]

Table 1 summarises the void swelling behaviour of Ni and FeNi, FeCoNi, CrCoNi, CrMnFeCoNi and CrFeCoNiPd irradiated with 3 MeV Ni ions to a peak dose of ~ 60 dpa at depth of 0-1800 nm from the surface, at 693 K, 773 K and 853 K. Note here there were slight differences in swelling reported in different studies and different values were all presented in the table. In general, CrCoNi exhibited very poor swelling resistance, even worse than FeNi, which again shows that alloying with Fe is more effective than Cr in terms of voids swelling resistance, and that increasing compositional complexity does not always lead to higher void swelling resistance. Yang et al. [92] suggested that slightly less pronounced void growth in CrFeCoNiPd compared with CrMnFeCoNi may be related to higher lattice distortion and a stronger binding energy between vacancies and constituent atoms in CrFeCoNiPd, which restricts vacancy mobility, promotes a higher recombination rate and leaves less free point defects. The mean local lattice distortion has been suggested [137] to be in the order: CrFeCoNi < CrMnFeCoNi < CrFeCoNiPd using X-ray total scattering experiments. DFT calculations also show less than 5% local distortion in CrFeCoNi and CrMnFeCoNi but $\sim 8\%$ lattice distortion in CrFeCoNiPd due to comparatively large bond distance of Pd-Pd neighbours. Modeling of Ni₈₀Mn₂₀ and Ni₈₀Pd₂₀ also showed that vacancy migration energies and the gap between vacancy and interstitial migration energy were surprisingly similar, suggesting that an alloying strategy based on the introduction of elements with larger atomic size differences into HEAs to increase local lattice

distortion as a means to modify vacancy mobility alone (and hence irradiation resistance), may not be effective. Moreover, larger atomic size mismatch may contribute to a tendency for the decomposition of any solid-solution phases that themselves are suggested to contribute to the irradiation resistance of HEAs [64, 138].

[Table 1 about here.]

Overall, the Cantor alloy showed the greatest resistance to void swelling of the alloys studied, with only 0.072% void swelling under Ni ion irradiation of up to 60 dpa, and a slower increase in swelling as temperature increased. A relatively condensed band of smaller voids in the Cantor alloy likely resulted from comparatively high recombination rates of vacancies and interstitials, and slower migration of large vacancy clusters. However, it will be useful, as the capability for a greater number of alloying elements is developed, to use simulations to assess if these interpretations are overly simplistic and if other intrinsic or extrinsic factors (grain size, impurities, dislocation density, etc) are of similar significance.

3.4. Gas bubbles

Extensive He production and retention from neutron induced transmutation reactions is a significant issue for materials to be applied in fast neutron environments. He atoms can diffuse rapidly, and may bond with vacancies, to form bubbles due to the limited intrinsic solubility of He in metallic systems. Hence, point defect behaviour, including mobility and concentration, are intimately linked with the problems that arise from He retention, and bubble formation, such as pronounced degradation in some macroscopic properties.

Ni and CrFeCoNi were irradiated under 190 keV He ions at room temperature using fluences ranging from $1 \times 10^{17} \text{ cm}^{-2}$ to $1 \times 10^{18} \text{ cm}^{-2}$ [139]. TEM showed that at $1 \times 10^{17} \text{ cm}^{-2}$, isolated, small He bubbles (1-2 nm) formed in CrFeCoNi while many small string-like suspected He bubbles formed in Ni. At $5 \times 10^{17} \text{ cm}^{-2}$, the average bubble size in Ni was $\sim 8 \text{ nm}$, which was similar to that of CrFeCoNi. At the highest dose of $1 \times 10^{18} \text{ cm}^{-2}$, numerous surface blisters and exfoliations occurred in Ni while there was only a slight surface blister in CrFeCoNi, in agreement with TEM investigations. CrFeCoNi was also more resistant to bubble coarsening than Ni during post-irradiation annealing. The smaller size but higher density of dislocations in CrFeCoNi compared with Ni may have served to retain the injected He into more disperse, smaller bubbles.

The temperature dependence on bubble formation in CrFeCoNi was investigated by implantation of 275 keV He ions at up to $5.14 \times 10^{16} \text{ cm}^{-2}$ fluence at 523 K, 573 K and 673 K [140], and by 2 MeV He ions at 773 K, 873 K and 973 K and at up to $1.52 \times 10^{16} \text{ cm}^{-2}$ fluence [141]. Generally, grain boundaries acted as sink traps for He to aggregate into bubbles and there was a He-depleted zone beside the grain boundary. The concurrently-produced self-interstitial atoms (SIAs) and vacancies were annihilated by existing bubbles and bubble evolution behaviour was dominated by the injected He ions. The average size of He bubbles increased whereas the He bubble density decreased with increasing temperature. At lower temperatures (523 K, 573 K and 673 K), He accumulation was slightly suppressed in the CrFeCoNi, with approximately 14.3%, 31.4% and 51.4% of the accumulated He ions precipitated into He bubbles at 523 K, 573 K and 673 K respectively. Fig. 22 displays cross-sectional

TEM images of Ni and CrFeCoNi at 773 K, 873 K and 973 K. There was a narrower distribution of He bubbles in CrFeCoNi than in Ni near the region with the highest concentration of incident He ions. He bubbles had a smaller diameter, larger number density and smaller volume fraction in CrFeCoNi compared with Ni, consistent with previous descriptions of the differences in the energy for point defect migration between Ni and CrFeCoNi, shown earlier in Fig. 4.

[Figure 23 about here.]

The effect of specific elements in Ni-based binary alloys on He bubble formation behaviour has also been investigated. $\text{Ni}_{80}\text{X}_{20}$ (X=Cr, Mn, Fe, Co, Ni and Pd) alloys were irradiated under 200 keV He ions at 773 K and $1 \times 10^{16} \text{ cm}^{-2}$ fluence [74]. Fig. 23 displays the migration (E_m^v , Fig. 23a) and formation (E_f^v , Fig. 23b) energies of vacancies and interstitials (E_m^i , Fig. 23c and E_f^i , Fig. 23d) of the binary alloys respectively. The combined experiments and DFT calculations show that alloying elements have a significant effect on He cavity formation. As seen in Fig. 23a and c, $\text{Ni}_{80}\text{Mn}_{20}$ exhibited the smallest energy gap between interstitial (E_m^i , mean value $\approx 0.3 \text{ eV}$) and vacancy migration energies (E_m^v , mean value $\approx 0.9 \text{ eV}$) of the binary alloys studied, which is likely to enhance vacancy-interstitial recombination rates and thus reduce bubble or cavity size in $\text{Ni}_{80}\text{Mn}_{20}$. In contrast, $\text{Ni}_{80}\text{Co}_{20}$ had the highest migration energy for vacancies (E_m^v , mean value $\approx 1.15 \text{ eV}$) and the lowest migration energy for interstitials (E_m^i , mean value $\approx 0.15 \text{ eV}$) and correspondingly $\text{Ni}_{80}\text{Co}_{20}$ showed the largest cavity size. The lower vacancy formation energy for $\text{Ni}_{80}\text{Pd}_{20}$ could result in a relatively wide and flat He cavity distribution over the irradiated range, and consistent with wider distribution of voids seen in CrFeCoNiPd, as

shown in Fig. 21.

[Figure 24 about here.]

Overall, investigations of He bubble formation and growth in the Cantor alloy and its derivatives are in the nascent stage, although there are some emerging useful observations, for example, CrFeCoNi exhibits higher resistance to bubble growth and bubble coarsening in post-annealing than Ni and He bubbles have a smaller diameter but higher number density in CrFeCoNi than in Ni. The formation and migration energies of vacancies and interstitials according to calculations are suggested to be the underlying reasons for the improved resistance to bubble growth of Cantor-like alloys.

4. Concluding remarks

The concept of high-entropy alloys is stimulating the investigation of many new alloy systems and new regions of multi-dimensional phase space. Among the many aspects under investigation, the irradiation damage and irradiation resistance of HEAs is relatively unexplored. Most work has focused on the CrMnFeCoNi alloy (the Cantor alloy) as a model system because it is a simple solid solution, unlike many HEAs that are often more microstructurally complex. It can also be processed to useful, multi-kg quantities using relatively straightforward metallurgical processes based on casting and forging [144].

This review has shown that the Cantor alloy and its derivatives exhibit irradiation resistance that is superior to more traditional dilute alloys of the same elements. The research methods have typically involved irradiation analogues

(electrons, heavy ions, and He) to fast neutron bombardment. Sophisticated microstructural analyses and computations have focused on comparative behaviour of single elements, binary alloys and the inter-related medium and high-entropy alloys. However, computational results including defect energies have been mostly limited to binary alloys, which may make it difficult to extrapolate findings to HEAs. Nonetheless, much of the trend-wise calculations of defect migration and formation energies are consistent with experimental investigations. Some key observations are:

The calculated point defect formation and migration energies of the Cantor alloy are described as a statistical distribution instead of the single values typically found in dilute alloys. There is a relatively small gap or even overlap between interstitial and vacancy migration energies, which will likely induce relatively high recombination rates and increase the possibility of defect annihilation, thus leaving less surviving defects.

Compared with Ni, which forms the basis of many alloys of practical use, retarded diffusion of interstitials and slightly faster migration of vacancies are expected in binary, CrCoNi and CrFeCoNi alloys due to higher interstitial migration energy and slightly lower vacancy migration energy.

The Cantor alloy has excellent phase stability against high dose heavy ion irradiation. Radiation-induced segregation (RIS) along grain boundaries in the Cantor alloy and its derivatives shows strong depletion of Mn and enrichment of Ni/Co, the magnitude of which is similar to or lower in extent than some fcc commercial alloys (304 stainless steels and Fe-Ni-Cr alloys). RIS along dislocation loops is significantly suppressed in the Cantor alloy, which may arise from retarded interstitial diffusion. Chemically biased diffusion may lead

to Ni/Co enrichment and Fe depletion in FeNi and CrFeCoNi due to the lower formation energy of Ni-Ni dumbbell defects.

There are interstitial-type, either elliptical Frank loops $1/3 \langle 111 \rangle$ or rhombus perfect loops $1/2 \langle 110 \rangle$, in the Cantor alloy and its derivatives under both electron and heavy ion irradiations at room and elevated temperature. There are some discrepancies regarding the size and density of loops as well as loop evolution, possibly due to different primary knock-on energy and errors introduced from counting procedures. Nonetheless, the Cantor alloy typically has a higher number density but much smaller size of dislocation loops compared with its binary and tertiary sub-systems, and conventional fcc alloys, which could suggest an extended incubation period for loop formation and retarded defect growth kinetics.

The Cantor alloy shows significantly enhanced resistance against void swelling compared with its derivatives and conventional fcc alloys, with only 0.072% void swelling under Ni ion irradiation up to 60 dpa. Large vacancy clusters were calculated to migrate much slower in binary and tertiary alloys than in Ni, which may underpin improved swelling resistance of the Cantor alloy.

A CrFeCoNi alloy was more resistant to the growth of He bubbles and bubble coarsening during post-annealing than Ni. There was a narrower distribution of He bubbles of smaller size, higher number density and smaller volume fraction in CrFeCoNi compared with Ni, which likely resulted from suppressed He diffusion.

The related HEAs, binary and tertiary sub-systems of the Cantor alloy fam-

ily so far have contained a significant concentration of Co and/or Ni. However, Co and Ni (along with many other elements) are generally considered undesirable in a real fast neutron reactor environment as they suffer from high levels of long-lasting induced radioactivity. The learning obtained from the Cantor system should be applied to HEAs comprising intrinsically low activation elements, and indeed this approach is fast gaining momentum (e.g. [44]). However, simple solid solutions in these alternative, generally much more refractory systems typically based on bcc metallic elements, are hard to find.

Despite its good phase stability, decomposition occurs in the Cantor alloy after long exposure to intermediate annealing temperatures (773-973 K). Further research is needed to examine the phase stability of the Cantor alloy and its derivatives after long-term exposure to combined radiation and temperature and, if necessary, to develop strategies to ensure greater phase stability under conditions of practical interest.

Research so far has mainly focused on comparing the radiation response of the Cantor alloy and its derivatives having a lower number of composing elements in order to elucidate the effect of compositional complexity on radiation resistance. The irradiation resistance of alloys with *more* alloying elements is not clear, and some preliminary studies of equiatomic alloys with more elements could at least be considered.

Lastly, the question whether and how well investigations of irradiation analogues (electrons and heavy ions) can represent fast neutron irradiation remains essentially unknown, and should be addressed in future research.

Appendix A. Acknowledgment

This work was supported by the UK Engineering and Physical Sciences Research Council through grants EP/P001645/1, EP/R006245/1 and EP/R021775/1.

References

- [1] Zhang, H., Huang, Y., Ning, H., Williams, C.A., London, A.J., Dawson, K., Hong, Z., Gorley, M.J., Grovenor, C.R., Tatlock, G.J., et al.: Processing and microstructure characterisation of oxide dispersion strengthened Fe-14Cr-0.4Ti-0.25Y₂O₃ ferritic steels fabricated by spark plasma sintering. *Journal of Nuclear Materials* **464**, 61–68 (2015)
- [2] Verma, A., Kumar, S., Grant, P.S., O'Reilly, K.A.Q.: Influence of cooling rate on the Fe intermetallic formation in an AA6063 Al alloy. *Journal of Alloys and Compounds* **555**, 274–282 (2013)
- [3] Cantor, B., Grant, P., Johnston, C.: *Automotive Engineering: Lightweight, Functional, and Novel Materials*, pp. 97–108. CRC Press, (2008)
- [4] Leyens, C., Peters, M.: *Titanium and titanium alloys: fundamentals and applications*, pp. 37–55. John Wiley, (2003)
- [5] Mi, J., Grant, P.S.: Modelling the shape and thermal dynamics of Ni superalloy rings during spray forming Part 1: Shape modelling-Droplet deposition, splashing and redeposition. *Acta Materialia* **56**(7), 1588–1596 (2008)
- [6] Reed, R.C.: *The superalloys: fundamentals and applications*, pp. 73–89. Cambridge university press, (2008)
- [7] He, J.Y., Wang, H., Huang, H.L., Xu, X.D., Chen, M.W., Wu, Y., Liu, X.J., Nieh, T.G., An, K., Lu, Z.P.: A precipitation-hardened high-entropy alloy with outstanding tensile properties. *Acta Materialia* **102**, 187–196 (2016)
- [8] Zhao, Y.H., Zhu, Y.T., Liao, X.Z., Horita, Z., Langdon, T.G.: Tailoring stacking fault energy for high ductility and high strength in ultrafine grained Cu and its

- alloy. Applied physics letters **89**(12), 121906 (2006)
- [9] Gludovatz, B., Hohenwarter, A., Catoor, D., Chang, E.H., George, E.P., Ritchie, R.O.: A fracture-resistant high-entropy alloy for cryogenic applications. Science **345**(6201), 1153 (2014)
- [10] Mordike, B.L.: Development of highly creep resistant magnesium alloys. Journal of Materials Processing Technology **117**(3), 391–394 (2001)
- [11] Huang, P.-K., Yeh, J.-W., Shun, T.-T., Chen, S.-K.: Multi-principal-element alloys with improved oxidation and wear resistance for thermal spray coating. Advanced Engineering Materials **6**(1-2), 74–78 (2004)
- [12] Xu, W., Birbilis, N., Sha, G., Wang, Y., Daniels, J.E., Xiao, Y., Ferry, M.: A high-specific-strength and corrosion-resistant magnesium alloy. Nature materials **14**(12), 1229–1235 (2015)
- [13] Smith, T., O'Reilly, K., Kumar, S., Stone, I.: Influence of grain-refiner addition on the morphology of Fe-bearing intermetallics in a semi-solid processed Al-Mg-Si alloy. Metallurgical and Materials Transactions A **44**(11), 4866–4871 (2013)
- [14] Devaraj, A., Joshi, V.V., Srivastava, A., Manandhar, S., Moxson, V., Duz, V.A., Lavender, C.: A low-cost hierarchical nanostructured beta-titanium alloy with high strength. Nature communications **7**(1), 1–8 (2016)
- [15] Williams, J.: Thermo-mechanical processing of high-performance Ti alloys: recent progress and future needs. Journal of materials processing technology **117**(3), 370–373 (2001)
- [16] Otto, F., Yang, Y., Bei, H., George, E.P.: Relative effects of enthalpy and entropy on the phase stability of equiatomic high-entropy alloys. Acta Materialia **61**(7), 2628–2638 (2013)
- [17] Zhou, Y.J., Zhang, Y., Wang, Y.L., Chen, G.L.: Solid solution alloys of Al Co Cr Fe Ni Ti x with excellent room-temperature mechanical properties. Applied physics letters **90**(18), 181904 (2007)

- [18] Zhang, Z., Zhang, H., Tang, Y., Ye, Y., Li, S., Bai, S.: Microstructure, mechanical properties and energetic characteristics of a novel high-entropy alloy HfZrTiTaO. *Materials & Design* **133**, 435–443 (2017)
- [19] Cantor, B., Chang, I.T.H., Knight, P., Vincent, A.J.B.: Microstructural development in equiatomic multicomponent alloys. *Materials Science and Engineering A* **375-377**, 213–218 (2004)
- [20] Yeh, J.W., Chen, S.K., Lin, S.J., Gan, J.Y., Chin, T.S., Shun, T.T., Tsau, C.H., Chang, S.Y.: Nanostructured High-Entropy Alloys with Multiple Principal Elements: Novel Alloy Design Concepts and Outcomes. *Advanced Engineering Materials* **6**(5), 299–303 (2004)
- [21] Zhang, Y., Stocks, G.M., Jin, K., Lu, C., Bei, H., Sales, B.C., Wang, L., Béland, L.K., Stoller, R.E., Samolyuk, G.D.: Influence of chemical disorder on energy dissipation and defect evolution in concentrated solid solution alloys. *Nature communications* **6**, 8736 (2015)
- [22] Pickering, E.J., Jones, N.G.: High-entropy alloys: a critical assessment of their founding principles and future prospects. *International Materials Reviews* **61**(3), 183–202 (2016)
- [23] Lu, C., Niu, L., Chen, N., Jin, K., Yang, T., Xiu, P., Zhang, Y., Gao, F., Bei, H., Shi, S.: Enhancing radiation tolerance by controlling defect mobility and migration pathways in multicomponent single-phase alloys. *Nature communications* **7**, 13564 (2016)
- [24] Senkov, O.N., Wilks, G.B., Scott, J.M., Miracle, D.B.: Mechanical properties of Nb₂₅Mo₂₅Ta₂₅W₂₅ and V₂₀Nb₂₀Mo₂₀Ta₂₀W₂₀ refractory high entropy alloys. *Intermetallics* **19**(5), 698–706 (2011)
- [25] Li, Z., Zhao, S., Ritchie, R.O., Meyers, M.A.: Mechanical properties of high-entropy alloys with emphasis on face-centered cubic alloys. *Progress in Materials Science* **102**, 296–345 (2019)

- [26] Gludovatz, B., Hohenwarther, A., Thurston, K.V., Bei, H., Wu, Z., George, E.P., Ritchie, R.O.: Exceptional damage-tolerance of a medium-entropy alloy CrCoNi at cryogenic temperatures. *Nature communications* **7**(1), 1–8 (2016)
- [27] Li, Z., Zhao, S., Ritchie, R.O., Meyers, M.A.: Mechanical properties of high-entropy alloys with emphasis on face-centered cubic alloys. *Progress in Materials Science* **102**, 296–345 (2019)
- [28] Miracle, D.B., Senkov, O.N.: A critical review of high entropy alloys and related concepts. *Acta Materialia* **122**, 448–511 (2017)
- [29] Zhang, Z., Mao, M.M., Wang, J., Gludovatz, B., Zhang, Z., Mao, S.X., George, E.P., Yu, Q., Ritchie, R.O.: Nanoscale origins of the damage tolerance of the high-entropy alloy CrMnFeCoNi. *Nature communications* **6**(1), 1–6 (2015)
- [30] Laplanche, G., Kostka, A., Horst, O.M., Eggeler, G., George, E.P.: Microstructure evolution and critical stress for twinning in the CrMnFeCoNi high-entropy alloy. *Acta Materialia* **118**, 152–163 (2016)
- [31] Zaddach, A.J., Niu, C., Koch, C.C., Irving, D.L.: Mechanical properties and stacking fault energies of NiFeCrCoMn high-entropy alloy. *Jom* **65**(12), 1780–1789 (2013)
- [32] Huang, S., Li, W., Lu, S., Tian, F., Shen, J., Holmström, E., Vitos, L.: Temperature dependent stacking fault energy of FeCrCoNiMn high entropy alloy. *Scripta Materialia* **108**, 44–47 (2015)
- [33] Egami, T., Guo, W., Rack, P.D., Nagase, T.: Irradiation Resistance of Multicomponent Alloys. *Metallurgical and Materials Transactions A* **45**(1), 180–183 (2014)
- [34] Hill, D.J.: Nuclear energy for the future. *Nature Materials* **7**(9), 680–682 (2008)
- [35] Zinkle, S.J., Was, G.S.: Materials challenges in nuclear energy. *Acta Materialia* **61**(3), 735–758 (2013)
- [36] Claudson, T.T., Barker, R.W., Fish, R.L.: The effects of fast flux irradiation on the

- mechanical properties and dimensional stability of stainless steel. Nuclear applications and technology **9**(1), 10–23 (1970)
- [37] Yvon, P., Carre, F.: Structural materials challenges for advanced reactor systems. Journal of Nuclear Materials **385**(2), 217–222 (2009)
- [38] Matijasevic, M., Almazouzi, A.: Effect of Cr on the mechanical properties and microstructure of Fe-Cr model alloys after irradiation. Journal of Nuclear Materials **377**(1), 147–154 (2008)
- [39] Murty, K.L., Charit, I.: Structural materials for Gen-IV nuclear reactors: Challenges and opportunities. Journal of Nuclear Materials **383**(1-2), 189–195 (2008)
- [40] Zinkle, S.J., Snead, L.L.: Designing radiation resistance in materials for fusion energy. Annual Review of Materials Research **44**, 241–267 (2014)
- [41] Rieth, M., Dudarev, S.L., Vicente, S.G.D., Aktaa, J., Ahlgren, T., Antusch, S., Armstrong, D.E.J., Balden, M., Baluc, N., Barthe, M.-F.: Recent progress in research on tungsten materials for nuclear fusion applications in Europe. Journal of Nuclear Materials **432**(1-3), 482–500 (2013)
- [42] Was, G.S., Ampornrat, P., Gupta, G., Teyseyre, S., West, E.A., Allen, T.R., Sridharan, K., Tan, L., Chen, Y., Ren, X.: Corrosion and stress corrosion cracking in supercritical water. Journal of Nuclear Materials **371**(1-3), 176–201 (2007)
- [43] Kareer, A., Waite, J.C., Li, B., Couet, A., Armstrong, D.E.J., Wilkinson, A.J.: ‘Low activation, refractory, high entropy alloys for nuclear applications’. Journal of Nuclear Materials **526**, 151744 (2019)
- [44] El-Atwani, O., Li, N., Li, M., Devaraj, A., Baldwin, J.K.S., Schneider, M.M., Sobieraj, D., Wróbel, J.S., Nguyen-Manh, D., Maloy, S.A.: Outstanding radiation resistance of tungsten-based high-entropy alloys. Science advances **5**(3), 2002 (2019)
- [45] Zhang, Y., Wang, X., Osetsky, Y.N., Tong, Y., Harrison, R., Donnelly, S.E., Chen,

- D., Wang, Y., Bei, H., Sales, B.C.: Effects of 3d electron configurations on helium bubble formation and void swelling in concentrated solid-solution alloys. *Acta Materialia* **181**, 519–529 (2019)
- [46] Zhao, S., Velisa, G., Xue, H., Bei, H., Weber, W.J., Zhang, Y.: Suppression of vacancy cluster growth in concentrated solid solution alloys. *Acta Materialia* **125**, 231–237 (2017)
- [47] Tsai, M.H., Yeh, J.W.: High-entropy alloys: a critical review. *Materials Research Letters* **2**(3), 107–123 (2014)
- [48] Zhang, Y., Zuo, T.T., Tang, Z., Gao, M.C., Dahmen, K.A., Liaw, P.K., Lu, Z.P.: Microstructures and properties of high-entropy alloys. *Progress in Materials Science* **61**, 1–93 (2014)
- [49] George, E.P., Raabe, D., Ritchie, R.O.: High-entropy alloys. *Nature Reviews. Materials* **4**(8) (2019)
- [50] Yang, T., Li, C., Zinkle, S., Zhao, S., Bei, H., & Zhang, Y: Irradiation responses and defect behavior of single-phase concentrated solid solution alloys. *Journal of Materials Research*, **33**(19), 3077-3091 (2018)
- [51] Zhang, Y., Zhao, S., Weber, W. J., Nordlund, K., Granberg, F., & Djurabekova, F.: Atomic-level heterogeneity and defect dynamics in concentrated solid-solution alloys. *Current Opinion in Solid State and Materials Science*, **21**(5), 221-237 (2017)
- [52] Zhang, Y., Jin, K., Xue, H., Lu, C., Olsen, R.J., Beland, L.K., Ullah, M.W., Zhao, S., Bei, H., Aidhy, D.S. and Samolyuk, G.D.: Influence of chemical disorder on energy dissipation and defect evolution in advanced alloys. *Journal of Materials Research*, **31**(16), 2363-2375 (2016)
- [53] Zhao, S., Zhang, Y., & Weber, W. J.: High Entropy Alloys: Irradiation (2020)
- [54] Pickering, E.J., Carruthers, A.W., Barron, P.J., Middleburgh, S.C., Armstrong,

D.E. and Gandy, A.S.: High-Entropy Alloys for Advanced Nuclear Applications. *Entropy*, **23**(1), 98 (2021)

- [55] Was, G.S.: Fundamentals of radiation materials science: metals and alloys, 208–215. Springer (2016)
- [56] Nagase, T., Anada, S., Rack, P.D., Noh, J.H., Yasuda, H., Mori, H., Egami, T.: Electron-irradiation-induced structural change in Zr-Hf-Nb alloy. *Intermetallics* **26**, 122–130 (2012)
- [57] Okamoto, P.R., Lam, N.Q., Rehn, L.E.: Physics of crystal-to-glass transformations. Elsevier (1999)
- [58] Motta, A.T.: Amorphization of intermetallic compounds under irradiation—A review. *Journal of Nuclear Materials* **244**(3), 227–250 (1997)
- [59] Nagase, T., Sanda, T., Nino, A., Qin, W., Yasuda, H., Mori, H., Umakoshi, Y., Szpunar, J.A.: MeV electron irradiation induced crystallization in metallic glasses: Atomic structure, crystallization mechanism and stability of an amorphous phase under the irradiation. *Journal of non-crystalline solids* **358**(3), 502–518 (2012)
- [60] Fu, E.G., Carter, J., Martin, M., Xie, G., Zhang, X., Wang, Y.Q., Littleton, R., Shao, L.: Electron irradiation-induced structural transformation in metallic glasses. *Scripta Materialia* **61**(1), 40–43 (2009)
- [61] Carter, J., Fu, E.G., Martin, M., Xie, G., Zhang, X., Wang, Y.Q., Wijesundera, D., Wang, X.M., Chu, W.-K., Shao, L.: Effects of Cu ion irradiation in Cu₅₀Zr₄₅Ti₅ metallic glass. *Scripta Materialia* **61**(3), 265–268 (2009)
- [62] Nagase, T., Rack, P.D., Noh, J.H., Egami, T.: In-situ TEM observation of structural changes in nano-crystalline CoCrCuFeNi multicomponent high-entropy alloy (HEA) under fast electron irradiation by high voltage electron microscopy (HVEM). *Intermetallics* **59**, 32–42 (2015)
- [63] Xia, S.Q., Yang, X., Yang, T.F., Liu, S., Zhang, Y.: Irradiation resistance in Alx-

- CoCrFeNi high entropy alloys. *Jom* **67**(10), 2340–2344 (2015)
- [64] Yang, T., Xia, S., Liu, S., Wang, C., Liu, S., Fang, Y., Zhang, Y., Xue, J., Yan, S., Wang, Y.: Precipitation behavior of Al x CoCrFeNi high entropy alloys under ion irradiation. *Scientific reports* **6**, 32146 (2016)
- [65] Granberg, F., Nordlund, K., Ullah, M.W., Jin, K., Lu, C., Bei, H., Wang, L.M., Djurabekova, F., Weber, W.J., Zhang, Y.: Mechanism of radiation damage reduction in equiatomic multicomponent single phase alloys. *Physical review letters* **116**(13), 135504 (2016)
- [66] Yamasaki, M., Kagao, S., Kawamura, Y.: Thermal diffusivity and conductivity of Zr₅₅Al₁₀Ni₅Cu₃₀ bulk metallic glass. *Scripta Materialia* **53**(1), 63–67 (2005)
- [67] Lee, J.I., Oh, H.S., Park, E.S.: Manipulation of σ_y/κ ratio in single phase FCC solid-solutions. *Applied Physics Letters* **109**(6), 061906 (2016)
- [68] Jin, K., Mu, S., An, K., Porter, W.D., Samolyuk, G.D., Stocks, G.M., Bei, H.: Thermophysical properties of Ni-containing single-phase concentrated solid solution alloys. *Materials & Design* **117**, 185–192 (2017)
- [69] Jin, K., Sales, B.C., Stocks, G.M., Samolyuk, G.D., Daene, M., Weber, W.J., Zhang, Y., Bei, H.: Tailoring the physical properties of Ni-based single-phase equiatomic alloys by modifying the chemical complexity. *Scientific reports* **6**, 20159 (2016)
- [70] Jin, K., Bei, H.: Single-phase concentrated solid-solution alloys: Bridging intrinsic transport properties and irradiation resistance. *Frontiers in Materials* **5**, 26 (2018)
- [71] Graves, R.S., Kollie, T.G., McElroy, D.L., Gilchrist, K.E.: The thermal conductivity of AISI 304L stainless steel. *International journal of thermophysics* **12**(2), 409–415 (1991)
- [72] Aidhy, D.S., Lu, C., Jin, K., Bei, H., Zhang, Y., Wang, L., Weber, W.J.: Point defect evolution in Ni, NiFe and NiCr alloys from atomistic simulations and irradiation

- experiments. *Acta Materialia* **99**, 69–76 (2015)
- [73] Lu, C., Jin, K., Béland, L.K., Zhang, F., Yang, T., Qiao, L., Zhang, Y., Bei, H., Christen, H.M., Stoller, R.E.: Direct observation of defect range and evolution in ion-irradiated single crystalline Ni and Ni binary alloys. *Scientific reports* **6**, 19994 (2016)
- [74] Fan, Z., Zhao, S., Jin, K., Chen, D., Osetskiy, Y.N., Wang, Y., Bei, H., More, K.L., Zhang, Y.: Helium irradiated cavity formation and defect energetics in Ni-based binary single-phase concentrated solid solution alloys. *Acta Materialia* **164**, 283–292 (2019)
- [75] Zhao, S., Stocks, G.M., Zhang, Y.: Defect energetics of concentrated solid-solution alloys from ab initio calculations: Ni 0.5 Co 0.5, Ni 0.5 Fe 0.5, Ni 0.8 Fe 0.2 and Ni 0.8 Cr 0.2. *Physical Chemistry Chemical Physics* **18**(34), 24043–24056 (2016)
- [76] Zhao, S., Egami, T., Stocks, G.M., Zhang, Y.: Effect of d electrons on defect properties in equiatomic NiCoCr and NiCoFeCr concentrated solid solution alloys. *Physical Review Materials* **2**(1), 013602 (2018)
- [77] Osetsky, Y.N., Béland, L.K., Stoller, R.E.: Specific features of defect and mass transport in concentrated fcc alloys. *Acta Materialia* **115**, 364–371 (2016)
- [78] Zhao, S., Osetsky, Y., Zhang, Y.: Preferential diffusion in concentrated solid solution alloys: NiFe, NiCo and NiCoCr. *Acta Materialia* **128**, 391–399 (2017)
- [79] Jin, K., Guo, W., Lu, C., Ullah, M.W., Zhang, Y., Weber, W.J., Wang, L., Poplawsky, J.D., Bei, H.: Effects of Fe concentration on the ion-irradiation induced defect evolution and hardening in Ni-Fe solid solution alloys. *Acta Materialia* **121**, 365–373 (2016)
- [80] Jiao, Z., Was, G.S.: Novel features of radiation-induced segregation and radiation-induced precipitation in austenitic stainless steels. *Acta Materialia* **59**(3), 1220–1238 (2011)

- [81] Allen, T.R., Busby, J.T., Was, G.S., Kenik, E.A.: On the mechanism of radiation-induced segregation in austenitic Fe-Cr-Ni alloys. *Journal of nuclear materials* **255**(1), 44–58 (1998)
- [82] Was, G.S., Wharry, J.P., Frisbie, B., Wirth, B.D., Morgan, D., Tucker, J.D., Allen, T.R.: Assessment of radiation-induced segregation mechanisms in austenitic and ferritic-martensitic alloys. *Journal of Nuclear Materials* **411**(1-3), 41–50 (2011)
- [83] Harries, D.R.: Neutron irradiation-induced embrittlement in type 316 and other austenitic steels and alloys. *Journal of Nuclear Materials* **82**(1), 2–21 (1979)
- [84] Bullough, R., Wood, M.H.: Mechanisms of radiation induced creep and growth. *journal of Nuclear Materials* **90**(1-3), 1–21 (1980)
- [85] Barnes, R.S.: Embrittlement of stainless steels and nickel-based alloys at high temperature induced by neutron radiation. *Nature* **206**(4991), 1307–1310 (1965)
- [86] Krishan, K.: Invited review article ordering of voids and gas bubbles in radiation environments. *Radiation Effects* **66**(3-4), 121–155 (1982)
- [87] Was, G.S.: *Irradiation-induced voids and bubbles*. Springer (2017)
- [88] Barr, C.M., Vetterick, G.A., Unocic, K.A., Hattar, K., Bai, X.-M., Taheri, M.L.: Anisotropic radiation-induced segregation in 316L austenitic stainless steel with grain boundary character. *Acta Materialia* **67**, 145–155 (2014)
- [89] Lu, Z., Faulkner, R.G., Was, G., Wirth, B.D.: Irradiation-induced grain boundary chromium microchemistry in high alloy ferritic steels. *Scripta Materialia* **58**(10), 878–881 (2008)
- [90] Fukuya, K.: Current understanding of radiation-induced degradation in light water reactor structural materials. *Journal of Nuclear Science and Technology* **50**(3), 213–254 (2013)

- [91] He, M.-R., Wang, S., Shi, S., Jin, K., Bei, H., Yasuda, K., Matsumura, S., Higashida, K., Robertson, I.M.: Mechanisms of radiation-induced segregation in CrFeCoNi- based single-phase concentrated solid solution alloys. *Acta Materialia* **126**, 182–193 (2017)
- [92] Yang, T., Lu, C., Velisa, G., Jin, K., Xiu, P., Zhang, Y., Bei, H., Wang, L.: Influence of irradiation temperature on void swelling in NiCoFeCrMn and NiCoFeCrPd. *Scripta Materialia* **158**, 57–61 (2019)
- [93] Lu, C., Yang, T., Jin, K., Gao, N., Xiu, P., Zhang, Y., Gao, F., Bei, H., Weber, W.J., Sun, K.: Radiation-induced segregation on defect clusters in single-phase concentrated solid-solution alloys. *Acta Materialia* **127**, 98–107 (2017)
- [94] Otto, F., Dlouhy, A., Pradeep, K.G., Kubá, M., Raabe, D., Eggeler, G., George, E.P.: Decomposition of the single-phase high-entropy alloy CrMnFeCoNi after prolonged anneals at intermediate temperatures. *Acta Materialia* **112**, 40–52 (2016)
- [95] Schuh, B., Mendez-Martin, F., Völker, B., George, E.P., Clemens, H., Pippan, R., Hohenwarter, A.: Mechanical properties, microstructure and thermal stability of a nanocrystalline CoCrFeMnNi high-entropy alloy after severe plastic deformation. *Acta Materialia* **96**, 258–268 (2015)
- [96] Pickering, E.J., Muñoz-Moreno, R., Stone, H.J., Jones, N.G.: Precipitation in the equiatomic high-entropy alloy CrMnFeCoNi. *Scripta Materialia* **113**, 106–109 (2016)
- [97] Barr, C.M., II, J.E.N., Unocic, K.A., Liu, J., Zhang, Y., Wang, Y., Taheri, M.L.: Exploring radiation induced segregation mechanisms at grain boundaries in equiatomic CoCrFeNiMn high entropy alloy under heavy ion irradiation. *Scripta Materialia* **156**, 80–84 (2018)
- [98] Barr, C.M., Barnard, L., Nathaniel, J.E., Hattar, K., Unocic, K.A., Szlurfarska, I., Morgan, D., Taheri, M.L.: Grain boundary character dependence of radiation-induced segregation in a model Ni-Cr alloy. *Journal of Materials Research* **30**(9),

1290–1299 (2015)

- [99] Vaidya, M., Pradeep, K.G., Murty, B.S., Wilde, G., Divinski, S.V.: Bulk tracer diffusion in CoCrFeNi and CoCrFeMnNi high entropy alloys. *Acta Materialia* **146**, 211–224 (2018)
- [100] Kumar, N.K., Li, C., Leonard, K.J., Bei, H., Zinkle, S.J.: Microstructural stability and mechanical behavior of FeNiMnCr high entropy alloy under ion irradiation. *Acta Materialia* **113**, 230–244 (2016)
- [101] Yang, T., Xia, S., Guo, W., Hu, R., Poplawsky, J.D., Sha, G., Fang, Y., Yan, Z., Wang, C., Li, C.: Effects of temperature on the irradiation responses of Al_{0.1}CoCrFeNi high entropy alloy. *Scripta Materialia* **144**, 31–35 (2018)
- [102] Piochaud, J.B., Klaver, T.P.C., Adjanor, G., Olsson, P., Domain, C., Becquart, C.S.: First-principles study of point defects in an fcc Fe-10Ni-20Cr model alloy. *Physical Review B* **89**(2), 024101 (2014)
- [103] Chen, W., Ding, X., Feng, Y., Liu, X., Liu, K., Lu, Z., Li, D., Li, Y., Liu, C.T., Chen, X.: Vacancy formation enthalpies of high-entropy FeCoCrNi alloy via first-principles calculations and possible implications to its superior radiation tolerance. *Journal of Materials Science & Technology* **34**(2), 355–364 (2018)
- [104] Middleburgh, S.C., King, D.M., Lumpkin, G.R., Cortie, M., Edwards, L.: Segregation and migration of species in the CrCoFeNi high entropy alloy. *Journal of alloys and compounds* **599**, 179–182 (2014)
- [105] Holmes, J.J., Bobbins, R.E., Brimhall, J.L.: Effect of fast reactor irradiation on the tensile properties of 304 stainless steel. *Journal of Nuclear Materials* **32**(2), 330–339 (1969)
- [106] Abe, F., Noda, T., Araki, H., Narui, M., Kayano, H.: Irradiation hardening and ductility loss of a low-activation 9Cr-1V ferritic steel at low temperatures. *Journal of Nuclear Materials* **166**(3), 265–277 (1989)

- [107] He, M., Wang, S., Jin, K., Bei, H., Yasuda, K., Matsumura, S., Higashida, K., Robertson, I.M.: Enhanced damage resistance and novel defect structure of CrFe-CoNi under in situ electron irradiation. *Scripta Materialia* **125**, 5–9 (2016)
- [108] Thomas, G., Washburn, J.: Precipitation of vacancies in metals. *Reviews of Modern Physics* **35**(4), 992 (1963)
- [109] Zhao, S., Stocks, G.M., Zhang, Y.: Stacking fault energies of face-centered cubic concentrated solid solution alloys. *Acta Materialia* **134**, 334–345 (2017)
- [110] Ding, Q., Fu, X., Chen, D., Bei, H., Gludovatz, B., Li, J., Zhang, Z., George, E.P., Yu, Q., Zhu, T.: Real-time nanoscale observation of deformation mechanisms in CrCoNi-based medium-to high-entropy alloys at cryogenic temperatures. *Materials Today* **25**, 21–27 (2019)
- [111] Was, G.S., Jiao, Z., Getto, E., Sun, K., Monterrosa, A.M., Maloy, S.A., Anderoglu, O., Sencer, B.H., Hackett, M.: Emulation of reactor irradiation damage using ion beams. *Scripta Materialia* **88**, 33–36 (2014)
- [112] Was, G.S.: Simulation of neutron irradiation effects with ions. *Fundamentals of Radiation Materials Science: Metals and Alloys*, 545–577 (2007)
- [113] Yang, T., Lu, C., Jin, K., Crespillo, M.L., Zhang, Y., Bei, H., Wang, L.: The effect of injected interstitials on void formation in self-ion irradiated nickel containing concentrated solid solution alloys. *Journal of Nuclear Materials* **488**, 328–337 (2017)
- [114] Shi, S., He, M.-R., Jin, K., Bei, H., Robertson, I.M.: Evolution of ion damage at 773K in Ni-containing concentrated solid-solution alloys. *Journal of Nuclear Materials* **501**, 132–142 (2018)
- [115] Gan, J., Simonen, E.P., Bruemmer, S.M., Fournier, L., Sencer, B.H., Was, G.S.: The effect of oversized solute additions on the microstructure of 316SS irradiated with 5 MeV Ni⁺⁺ ions or 3.2 MeV protons. *Journal of nuclear materials* **325**(2-3), 94–106 (2004)

- [116] Okita, T., Sato, T., Sekimura, N., Iwai, T., Garner, F.A.: The synergistic influence of temperature and displacement rate on microstructural evolution of ion-irradiated Fe-15Cr-16Ni model austenitic alloy. *Journal of nuclear materials* **367**, 930–934 (2007)
- [117] Etienne, A., Hernández-Mayoral, M., Genevois, C., Radiguet, B., Pareige, P.: Dislocation loop evolution under ion irradiation in austenitic stainless steels. *Journal of nuclear materials* **400**(1), 56–63 (2010)
- [118] Muroga, T., Yoshida, N., Garner, F.A.: The influence of nickel content on microstructures of Fe-Cr-Ni austenitic alloys irradiated with nickel ions (1990)
- [119] McDonald, S.G., Taylor, A.: Void swelling behavior of types 304 and 316 stainless steel irradiated with 4-MeV Ni⁺ ions. ASTM International (1973)
- [120] Jin, H., Ko, E., Lim, S., Kwon, J.: Effects of helium and hydrogen on radiation-induced microstructural changes in austenitic stainless steel. *Nuclear Instruments and Methods in Physics Research Section B: Beam Interactions with Materials and Atoms* **359**, 69–74 (2015)
- [121] Shiraishi, K., Fukai, K., Yagi, E.: Damage profiles in a stainless steel irradiated with Ar and N ions. *Journal of nuclear materials* **179**, 550–553 (1991)
- [122] Wood, S., Spitznagel, J.A., Choyke, W.J., Doyle, N.J., McGruer, J.N., Townsend, J.R.: Microstructural development in dual-ion-bombarded 316 stainless steel. ASTM International (1981)
- [123] Xu, Q., Watanabe, H., Yoshida, N.: Microstructural evolution in FeCrNi alloy irradiated with Ni ion under varying temperature. *Journal of nuclear materials* **233**, 1057–1061 (1996)
- [124] Lee, E.H., Byun, T.S., Hunn, J.D., Yoo, M.H., Farrell, K., Mansur, L.K.: On the origin of deformation microstructures in austenitic stainless steel: part I—microstructures. *Acta materialia* **49**(16), 3269–3276 (2001)
- [125] Huang, H.F., Li, J.J., Li, D.H., Liu, R.D., Lei, G.H., Huang, Q., Yan, L.: TEM,

- XRD and nanoindentation characterization of Xenon ion irradiation damage in austenitic stainless steels. *Journal of Nuclear Materials* **454**(1-3), 168–172 (2014)
- [126] Williams, T.M.: The effect of soluble carbon on void swelling and low dose dislocation structures in type 316 austenitic stainless steel irradiated with 46.5 MeV Ni⁶⁺ ions. *Journal of Nuclear Materials* **88**(2-3), 217–225 (1980)
- [127] Hudson, J.A.: Void formation in solution-treated AISI 316 and 321 stainless steels under 46.5 MeV Ni⁶⁺ irradiation. *Journal of Nuclear Materials* **60**(1), 89–106 (1976)
- [128] Williams, T.M.: Interstitial loop nucleation and growth in solution-treated type 316 stainless steel irradiated to low doses with 22 MeV C²⁺ and 46.5 MeV Ni⁶⁺ ions. *Journal of Nuclear Materials* **79**(1), 28–42 (1979)
- [129] Chen, W., Liu, X., Chen, Y., Yeh, J., Tseng, K., Natesan, K.: Irradiation effects in high entropy alloys and 316H stainless steel at 300° C. *Journal of Nuclear Materials* **510**, 421–430 (2018)
- [130] Sencer, B.H., Garner, F.A.: Compositional and temperature dependence of void swelling in model Fe-Cr base alloys irradiated in the EBR-II fast reactor. *Journal of nuclear materials* **283**, 164–168 (2000)
- [131] Garner, F.A., Toloczko, M.B.: Irradiation creep and void swelling of austenitic stainless steels at low displacement rates in light water energy systems. *Journal of nuclear materials* **251**, 252–261 (1997)
- [132] Garner, F.A., Toloczko, M.B., Sencer, B.H.: Comparison of swelling and irradiation creep behavior of fcc-austenitic and bcc-ferritic/martensitic alloys at high neutron exposure. *Journal of Nuclear Materials* **276**(1-3), 123–142 (2000)
- [133] Jin, K., Lu, C., Wang, L.M., Qu, J., Weber, W.J., Zhang, Y., Bei, H.: Effects of compositional complexity on the ion-irradiation induced swelling and hardening in Ni-containing equiatomic alloys. *Scripta Materialia* **119**, 65–70 (2016)

- [134] Packan, N.H., Farrell, K.: Radiation-induced swelling in an austenitic alloy: Observations and interpretation of the effects of helium. *Nuclear Technology-Fusion* **3**(3), 392–404 (1983)
- [135] Yang, Tai Ni., Wang, Lumin., Misra, Amit., Gao, Fei., and Was, Gary.: *The Effect of Principal Elements on Defect Evolution in Single-Phase Solid Solution Ni Alloys*. ProQuest Dissertations and Theses. Web (2018)
- [136] Lu, C., Yang, T., Jin, K., Velisa, G., Xiu, P., Peng, Q., Gao, F., Zhang, Y., Bei, H., Weber, W.J., *et al.*: Irradiation effects of medium-entropy alloy NiCoCr with and without pre-indentation. *Journal of Nuclear Materials* **524**, 60–66 (2019)
- [137] Tong, Y., Velisa, G., Zhao, S., Guo, W., Yang, T., Jin, K., Lu, C., Bei, H., Ko, J.Y.P., Pagan, D.C.: Evolution of local lattice distortion under irradiation in medium- and high-entropy alloys. *Materialia* **2**, 73–81 (2018)
- [138] Xia, S., Gao, M.C., Yang, T., Liaw, P.K., Zhang, Y.: Phase stability and microstructures of high entropy alloys ion irradiated to high doses. *Journal of Nuclear Materials* **480**, 100–108 (2016)
- [139] Yan, Z., Liu, S., Xia, S., Zhang, Y., Wang, Y., Yang, T.: He behavior in Ni and Ni-based equiatomic solid solution alloy. *Journal of Nuclear Materials* **505**, 200–206 (2018)
- [140] Chen, D., Tong, Y., Li, H., Wang, J., Zhao, Y.L., Hu, A., Kai, J.J.: Helium accumulation and bubble formation in FeCoNiCr alloy under high fluence He⁺ implantation. *Journal of Nuclear Materials* **501**, 208–216 (2018)
- [141] Chen, D., Zhao, S., Sun, J., Tai, P., Sheng, Y., Zhao, Y., Yeli, G., Lin, W., Liu, S., Kai, W.: Diffusion controlled helium bubble formation resistance of FeCoNiCr high-entropy alloy in the half-melting temperature regime. *Journal of Nuclear Materials* **526**, 151747 (2019)
- [142] Urban, K., Wilkens, M.: Growth of defect clusters in thin nickel foils during electron irradiation. II. Temperature dependence of the growth rate of interstitial

loops. *physica status solidi (a)* **6**(1), 173–185 (1971)

- [143] Lu, C., Yang, T., Jin, K., Velisa, G., Xiu, P., Song, M., Peng, Q., Gao, F., Zhang, Y., Bei, H.: Enhanced void swelling in NiCoFeCrPd high-entropy alloy by indentation-induced dislocations. *Materials Research Letters* **6**(10), 584–591 (2018)
- [144] Zhao, S., Li, Z., Zhu, C., Yang, W., Zhang, Z., Armstrong, D.E.J, Grant, P.S., Ritchie, R.O. and Meyers, M.A.: Amorphization in extreme deformation of the CrMnFeCoNi high-entropy alloy. *Science advances*, **7**(5), p.eabb3108 (2021)

List of Figures

- A.1 (a) and (b) Rutherford backscattering yield spectra as a function of distance from the irradiated surface along the (001) direction in which pristine and amorphous spectra indicated the boundary of damage-free and fully damaged states. Decreasing backscattering yield suggested radiation resistance of $\text{CrFeCoNi} > \text{FeNi} > \text{CoNi} > \text{Ni}$. TEM images of (c) Ni, (d) CoNi and (e) FeNi samples irradiated using 3 MeV Au ions to a fluence of $2 \times 10^{13} \text{ cm}^{-2}$; the scale bar is 40 nm. (f) Defect distribution in Ni, CoNi and FeNi. Figure adapted from Zhang et al. [21] 45
- A.2 Thermal conductivity of the Cantor alloy and its derivatives, and several commercial alloys and BMGs in the temperature range 0 to 1000 K [66–69]. Figure adapted from Jin et al. [70] 46
- A.3 (a) Defect structures in Ni and FeNi at a dose of 0.5 dpa. The displaced fcc atoms are removed to show only atoms that are part of the defect structure. (b) Average cluster size distribution at an irradiation dose from 0.4 dpa to 0.57 dpa in Ni, FeNi and CrCoNi with the inset showing the same distribution grouped by cluster diameter. Figure adapted from Granberg et al. [65] 47
- A.4 Migration energy of (a) an interstitial (b) a vacancy in FeNi determined from ab initio calculations; migration energy of an interstitial and a vacancy in (c) CrCoNi and (d) CrFeCoNi. The black dashed lines represent the migration energies of interstitials and vacancies in pure Ni. Figure adapted from Zhao et al. [75, 76] 48
- A.5 TEM images of (a) Ni (b) $\text{Ni}_{80}\text{Fe}_{20}$ and (c) FeNi irradiated at a

fluence of $5 \times 10^{15} \text{ cm}^{-2}$ in which typical SFT and dislocation loops are marked with red circles and blue arrows. With increasing concentration of Fe, there was a decrease in defect size.

(d) Defect size distribution in Ni, $\text{Ni}_{80}\text{Fe}_{20}$ and FeNi after irradiation at a depth of 350 nm corresponding to the area with a peak dose of 6.5 dpa. Figure adapted from Jin et al. [79] 49

A.6 (a) Annular dark-field (ADF) scanning transmission electron microscopy (STEM) image of electron-irradiated Cantor alloy showing $\langle 110 \rangle$ -oriented modulated structure due to spinodal decomposition, and (b) corresponding selected area electron diffraction (SAED) along the $[001]$ zone axis with an enlarged view highlighting $\{100\}$ and $\{110\}$ families of ordering. (c) Simulated SAED produced by a mixture of L_{10} (NiMn)-type ordering in all three orientations agreeing well with experimental observation in (b). Figure adapted from He et al. [91] 50

A.7 (a) EDX maps superimposed on a STEM bright field (BF) image of the Cantor alloy after annealing at 773 K for 500 days with three precipitates. Corresponding SAED images superimposed with simulated diffraction patterns (red circles) of (b) L_{10} -type NiMn, (c) bcc Cr-rich solid solution, and (d) B2-type FeCo. Figure adapted from Otto et al. [94] 51

A.8 (a) Representative irradiation-induced segregation profiles from a STEM-EDX linescan at a random high angle GB in the Cantor alloy irradiated with 3 MeV Ni ions at 773 K and 2 dpa. (b) Comparison of the compositional change along GBs and the

matrix between the Cantor alloy and conventional fcc alloys (304 high and commercial purity [80], model Ni-Cr alloys [81, 98], model Fe-Ni-Cr alloys [81]). Figure adapted from Barr et al. [97] 52

A.9 (a) STEM-BF image of a dislocation loop in the Cantor alloy; (b) high-resolution HAADF image enlarged from the region marked by the red box showing an interstitial-type Frank loop. Element lines-can profiles across the dislocation loops in (c) FeNi, (d) FeCoNi, (e) CrFeCoNi and (f) CrMnFeCoNi. Figure adapted from Lu et al. [93] 53

A.10 Formation energy of a [100] dumbbell in (a) FeNi, (c) CrCoNi and (e) CrFeCoNi determined by ab initio calculations (upper column); formation energy of a vacancy in (b) FeNi, (d) CrCoNi and (f) CrFeCoNi (lower column). The black dashed lines represent the formation energies of interstitials and vacancies in Ni. The formation energy of interstitials in Ni is beyond the scale of (c) and (e). Figure adapted from Zhao et al. [75, 76] 54

A.11 Growth behaviour of dislocation loops in a CrFeCoNi irradiated by 1250 keV electrons at 673 K. Weak beam dark field (WBDF) images showing the growth of (a) a Frank interstitial loop and (b) a perfect loop taken under **g,3.1g** condition. (c) Major axis length of Frank loops (green) and perfect loops (purple) as a function of damage level. Dash lines are fitting curves by power law with black lines representing linear growth of Frank loops in Ni ion irradiated by 650 keV electron beam at 693 K. [142] Figure adapted from He et al. [107] 55

A.12 Cross-sectional TEM images showing the distribution of dislocations, dislocation loops and voids in Ni, CoNi, FeNi, CrFeCoNi and CrMnFeCoNi irradiated with 1.5 or 3 MeV Ni ions at different fluences. Scale bar is 100 nm. Figure adapted from Lu et al. [23]

56

A.13 Kinetic two-beam condition BF TEM images of dislocation loops in (a) FeNi, (b) FeCoNi, (c) CrFeCoNi and (d) CrMnFeCoNi irradiated with 3 MeV Ni ions at 773 K and up to 38 ± 5 dpa. Perfect, faulted and edge-on faulted loops are marked by blue, yellow and red arrows respectively [92].

57

A.14 (a) Loop density; (b) loop size distribution; (c) average diameter of loops and (d) fraction of $1/3 \langle 111 \rangle$ faulted loops in FeNi, FeCoNi, CrFeCoNi and CrMnFeCoNi irradiated with 3 MeV Ni ions at 773 K and up to 38 ± 5 dpa [93]

58

A.15 (a) Defect density and (b) defect average size as a function of ion dose in Ni, FeNi, CoNi, CrCoNi, CrFeCoNi, CrMnFeCoNi and CrFeCoNiPd irradiated with 1 MeV Kr ions at a temperature of 773 K and from 0.1 to 2 dpa. Figure adapted from Shi et al. [114]

59

A.16 Comparison of loop density versus irradiation temperature in $\text{Cr}_{18}\text{Mn}_{27}\text{Fe}_{27}\text{Ni}_{28}$ and conventional Fe-Cr-Ni austenitic alloys [115–128], irradiated at similar conditions [100]

60

A.17 BF TEM images and corresponding SAED patterns of a $\text{Al}_{0.1}\text{CrFeCoNi}$ irradiated with 3 MeV Au ions at different temperatures from 523 K to 923 K. Perfect loops and SFTs are marked by blue arrows and green circles [101]. Defect density

decreased but defect size increased with increasing irradiation temperature. 61

A.18 WBDF (top) and BF (bottom) images of (a) 316H stainless steel, (b) CrMnFeCoNi and (c) Al_{0.3}CrFeCoNi irradiated with 1 MeV Kr ions at 573 K and different doses. (d) The loop density and (e) average size of loops as a function of dose in the three alloys respectively. Figure adapted from Chen et al [129] 62

A.19 (a) Optical profilometer measurements of void swelling in Ni, CoNi, CrCoNi and CrMnFeCoNi. (b) Step height change of each alloy after irradiation. Cross-sectional TEM images showing different sizes and density of voids in (c) Ni, (d) CoNi, (e) CrCoNi and (f) CrMnFeCoNi. Figure adapted from Jin et al [132]. 63

A.20 (a) Cross-sectional TEM images of Ni, CoNi, FeNi and CrFeCoNi irradiated with 1.5 MeV Ni ions to $3 \times 10^{15} \text{ cm}^{-2}$ at 773 K with enlarged area marked by a dotted blue box; scale bar in the inset figures is 50 nm. (b) cross-sectional TEM images of Ni, FeNi, FeCoNi and CrMnFeCoNi irradiated with 3 MeV Ni ions to $5 \times 10^{16} \text{ cm}^{-2}$ at 773 K [23], showing reduced void formation with increasing compositional complexity 64

A.21 The comparison of swelling behaviour between the Cantor alloy, its derivatives, and conventional steels (e.g. 316SS, FeCr15Ni16) under similar conditions [115,116,134,135]. Average size (nm, square marks) and the number density of voids (10^{20} m^{-3} , circles) are displayed as a function of overall swelling (%) in different materials. The irradiation conditions corresponding to each

data point were included on the right where half hollow marks represented data obtained at the irradiation of ~10 dpa and solid marks represented data obtained at the irradiation of 50-70 dpa. 65

A.22 Cross-sectional TEM images of CrCoNi, CrMnFeCoNi and CrFeCoNiPd irradiated with 3 MeV Ni ions at (a) 693 K, (b) 773 K and (c) 853 K, to a fluence of $5 \times 10^{16} \text{ cm}^{-2}$, showing dependence of void formation on composition and temperature. Figure adapted from Lu et al. and Yang et al. [92, 136] 66

A.23 (a) The Stopping and Range of Ions in Matter (SRIM) simulated ion radiation damage and incident He concentration profiles overlapped with a cross-section TEM image. The red dashed box indicates the peak damage region from where (b) was obtained. (b) Cross-sectional TEM images of Ni and CrFeCoNi irradiated by 2 MeV He ions at up to $1.52 \times 10^{16} \text{ cm}^{-2}$ fluence and (a) 773 K, (b) 873 K and (c) 973 K [141]. 67

A.24 (a) The migration (E_m^v) and (b) formation (E_f^v) energies of vacancies and (c) and (d) of interstitials (E_m^i and E_f^i) of $\text{Ni}_{80}\text{X}_{20}$ (X=Cr, Mn, Fe, Co, Ni and Pd) binary alloys from DFT calculations. The dashed lines represent the energies in Ni. Figure adapted from Fan et al. [69] 68

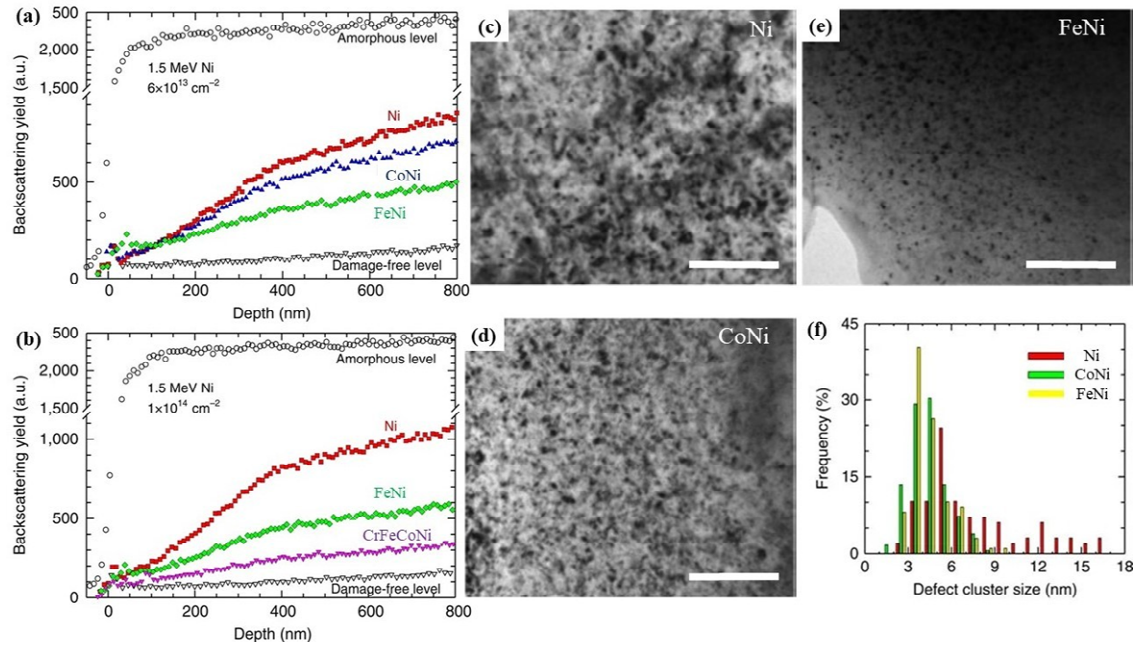


Figure A.1: (a) and (b) Rutherford backscattering yield spectra as a function of distance from the irradiated surface along the (001) direction in which pristine and amorphous spectra indicated the boundary of damage-free and fully damaged states. Decreasing backscattering yield suggested radiation resistance of $\text{CrFeCoNi} > \text{FeNi} > \text{CoNi} > \text{Ni}$. TEM images of (c) Ni, (d) CoNi and (e) FeNi samples irradiated using 3 MeV Au ions to a fluence of $2 \times 10^{13} \text{ cm}^{-2}$; the scale bar is 40 nm. (f) Defect distribution in Ni, CoNi and FeNi. Figure adapted from Zhang et al. [21]

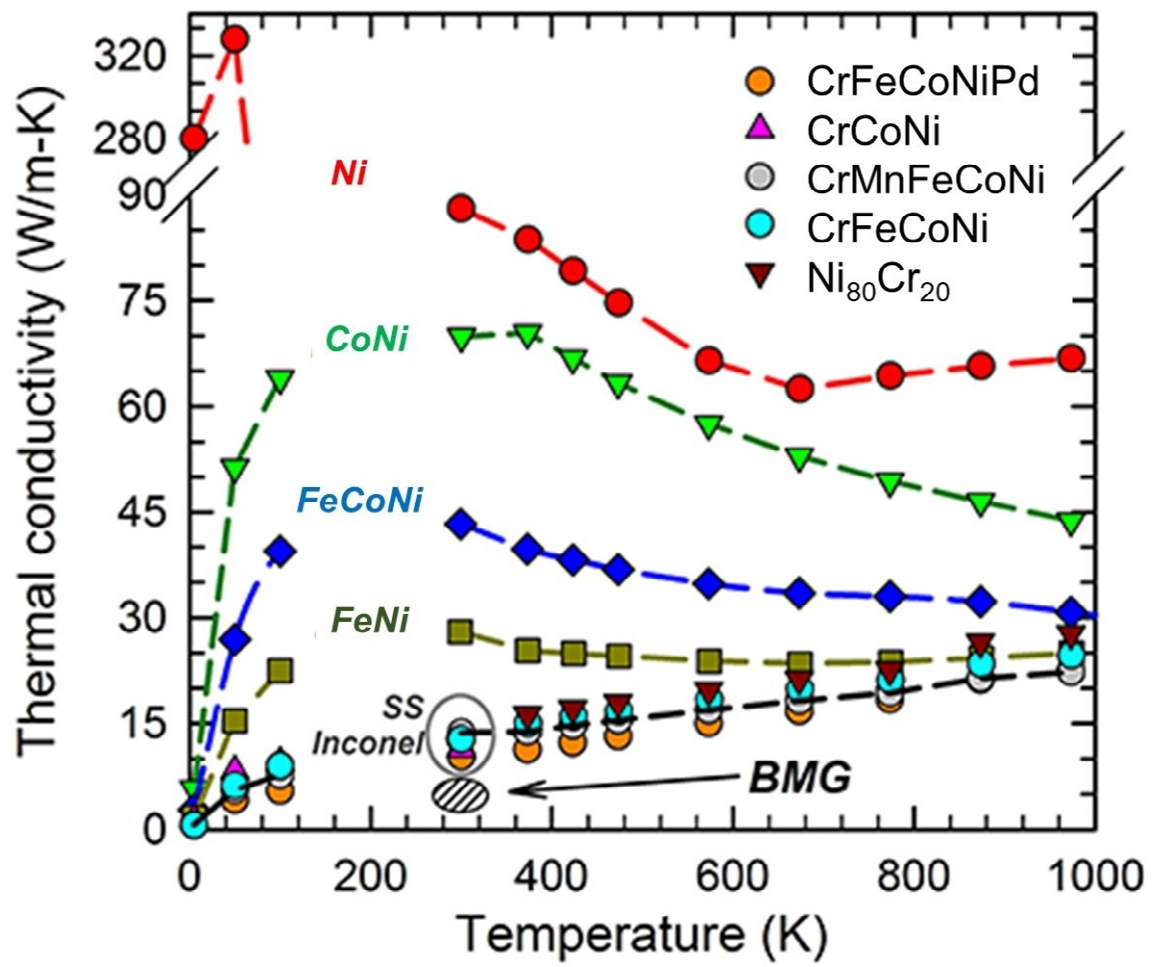


Figure A.2: Thermal conductivity of the Cantor alloy and its derivatives, and several commercial alloys and BMGs in the temperature range 0 to 1000 K [65–69]. Figure adapted from Jin et al. [70]

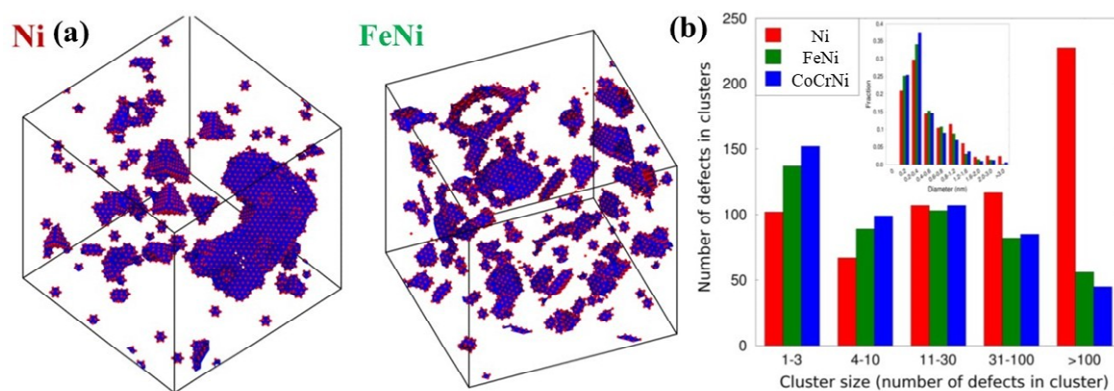


Figure A.3: (a) Defect structures in Ni and FeNi at a dose of 0.5 dpa. The displaced fcc atoms are removed to show only atoms that are part of the defect structure. (b) Average cluster size distribution at an irradiation dose from 0.4 dpa to 0.57 dpa in Ni, FeNi and CrCoNi with the inset showing the same distribution grouped by cluster diameter. Figure adapted from Granberg et al. [65]

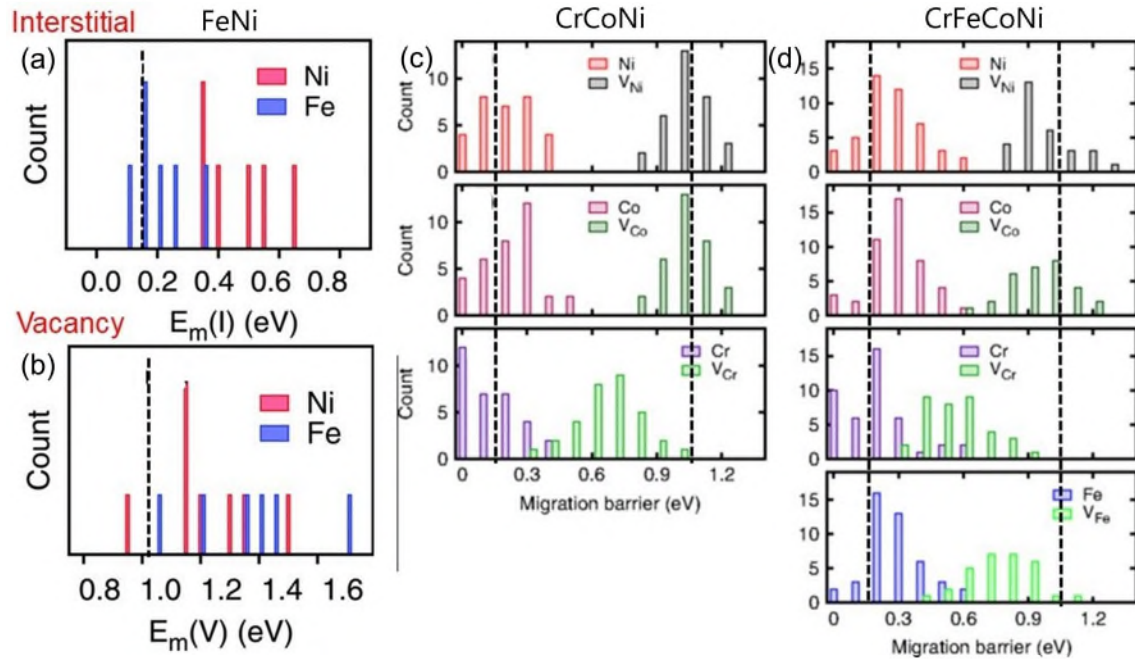


Figure A.4: Migration energy of (a) an interstitial (b) a vacancy in FeNi determined from ab initio calculations; migration energy of an interstitial and a vacancy in (c) CrCoNi and (d) CrFeCoNi. The black dashed lines represent the migration energies of interstitials and vacancies in pure Ni. Figure adapted from Zhao et al. [75, 76]

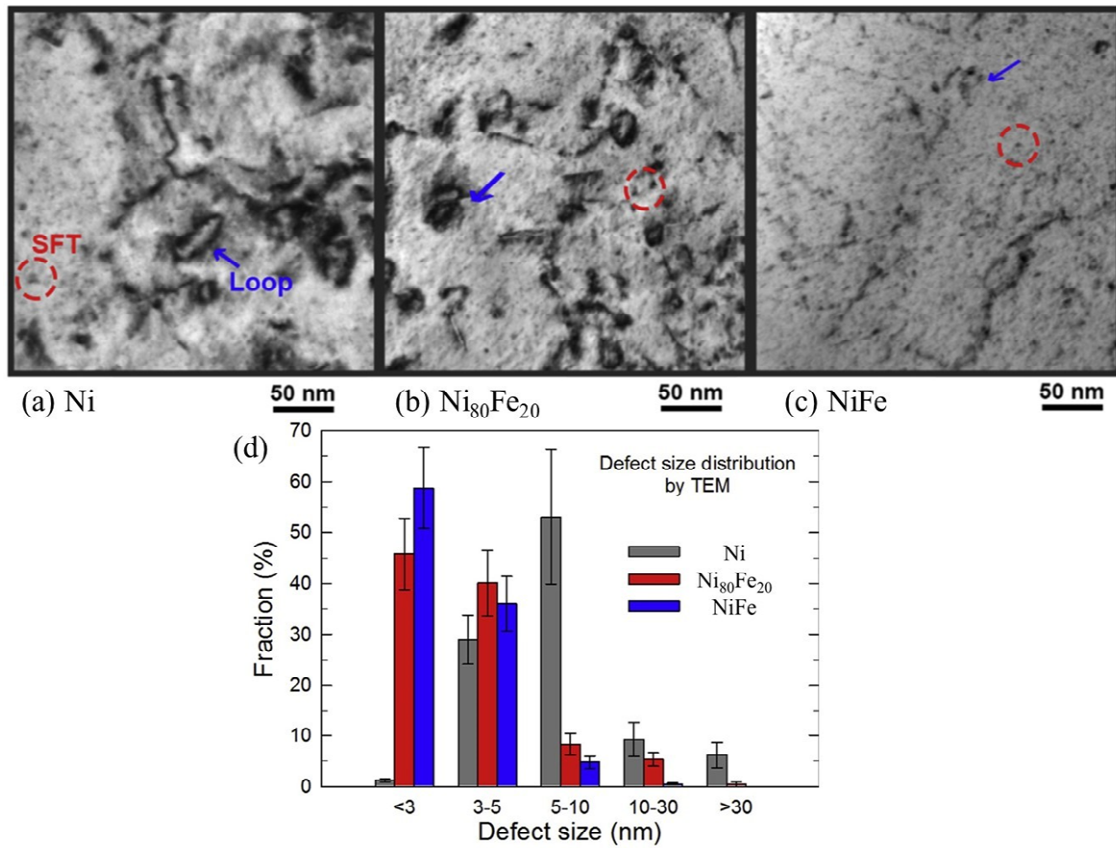


Figure A.5: TEM images of (a) Ni (b) Ni₈₀Fe₂₀ and (c) FeNi irradiated at a fluence of $5 \times 10^{15} \text{ cm}^{-2}$ in which typical SFT and dislocation loops are marked with red circles and blue arrows. With increasing concentration of Fe, there was a decrease in defect size. (d) Defect size distribution in Ni, Ni₈₀Fe₂₀ and FeNi after irradiation at a depth of 350 nm corresponding to the area with a peak dose of $\sim 6.5 \text{ dpa}$. Figure adapted from Jin et al. [79]

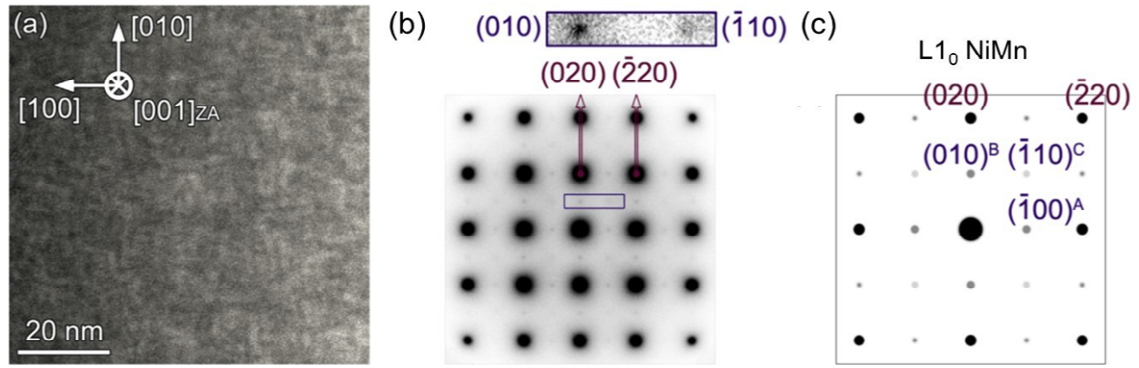


Figure A.6: (a) Annular dark-field (ADF) scanning transmission electron microscopy (STEM) image of electron-irradiated Cantor alloy showing $\langle 110 \rangle$ -oriented modulated structure due to spinodal decomposition, and (b) corresponding selected area electron diffraction (SAED) along the $[001]$ zone axis with an enlarged view highlighting $\{100\}$ and $\{110\}$ families of ordering. (c) Simulated SAED produced by a mixture of $L1_0$ (NiMn)-type ordering in all three orientations agreeing well with experimental observation in (b). Figure adapted from He et al. [91]

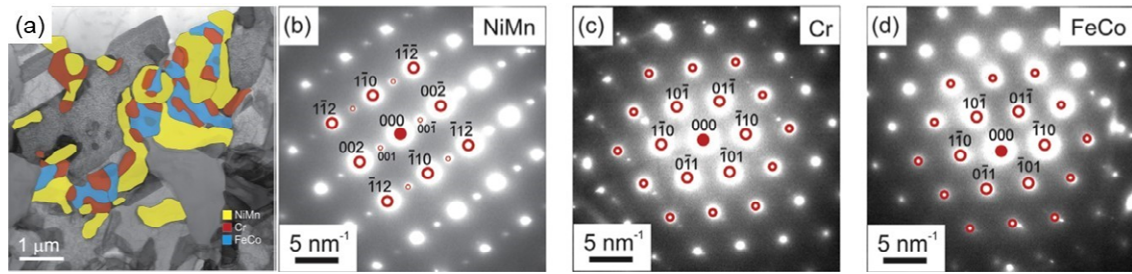


Figure A.7: (a) EDX maps superimposed on a STEM bright field (BF) image of the Cantor alloy after annealing at 773 K for 500 days with three precipitates. Corresponding SAED images superimposed with simulated diffraction patterns (red circles) of (b) L_{10} -type NiMn, (c) bcc Cr-rich solid solution, and (d) B2-type FeCo. Figure adapted from Otto et al. [94]

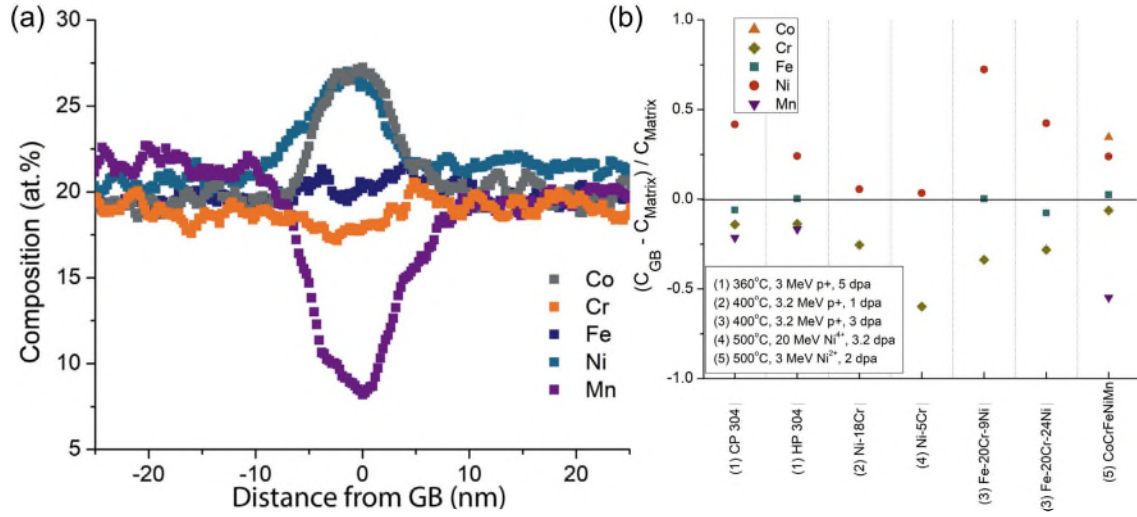


Figure A.8: (a) Representative irradiation-induced segregation profiles from a STEM-EDX linescan at a random high angle GB in the Cantor alloy irradiated with 3 MeV Ni ions at 773 K and 2 dpa. (b) Comparison of the compositional change along GBs and the matrix between the Cantor alloy and conventional fcc alloys (304 high and commercial purity [80], model Ni-Cr alloys [81, 98], model Fe-Ni-Cr alloys [81]). Figure adapted from Barr et al. [97]

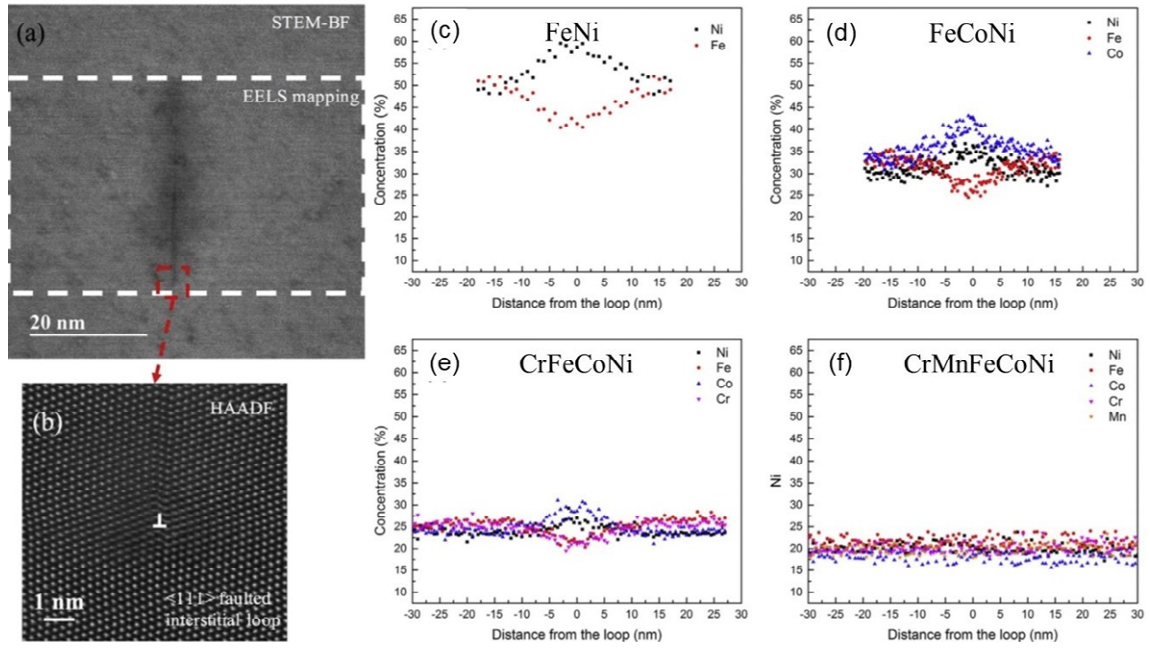


Figure A.9: (a) STEM-BF image of a dislocation loop in the Cantor alloy; (b) high-resolution HAADF image enlarged from the region marked by the red box showing an interstitial-type Frank loop. Element line-scan profiles across the dislocation loops in (c) FeNi, (d) FeCoNi, (e) CrFeCoNi and (f) CrMnFeCoNi. Figure adapted from Lu et al. [93]

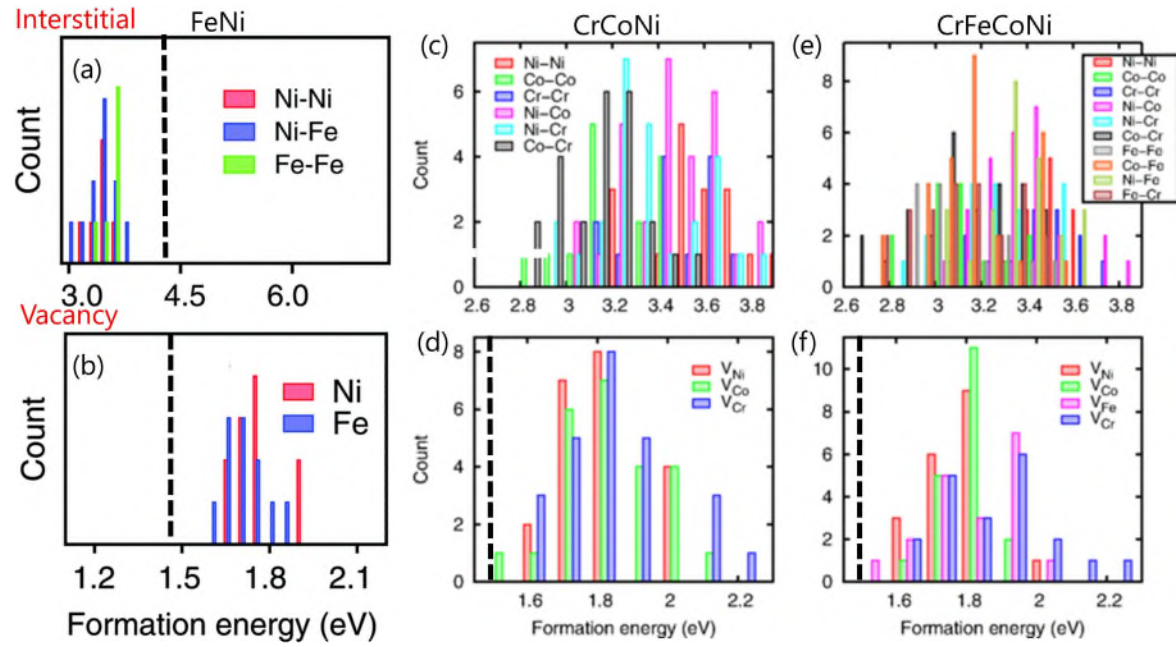


Figure A.10: Formation energy of a [100] dumbbell in (a) FeNi, (c) CrCoNi and (e) CrFeCoNi determined by ab initio calculations (upper column); formation energy of a vacancy in (b) FeNi, (d) CrCoNi and (f) CrFeCoNi (lower column). The black dashed lines represent the formation energies of interstitials and vacancies in Ni. The formation energy of interstitials in Ni is beyond the scale of (c) and (e). Figure adapted from Zhao et al. [75, 76]

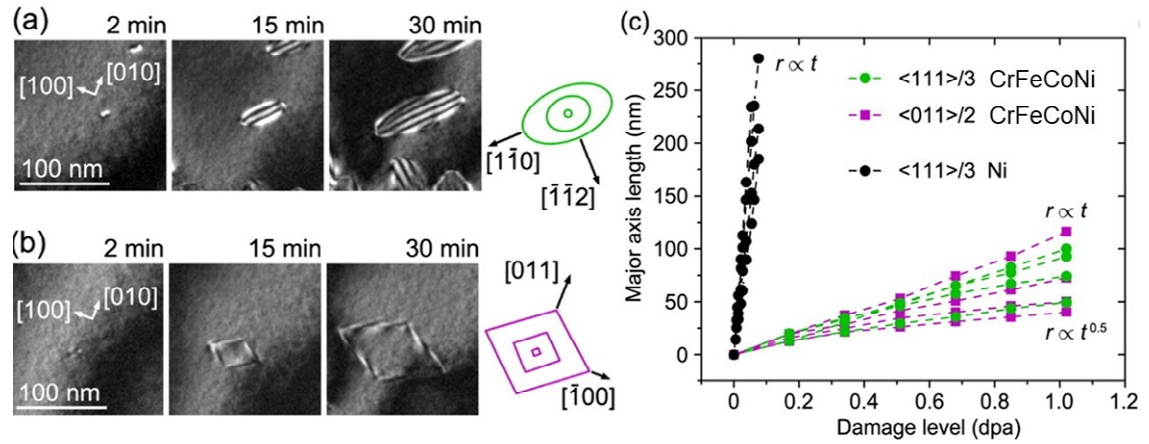


Figure A.11: Growth behaviour of dislocation loops in a CrFeCoNi irradiated by 1250 keV electrons at 673 K. Weak beam dark field (WDBF) images showing the growth of (a) a Frank interstitial loop and (b) a perfect loop taken under $\mathbf{g}, 3.1\mathbf{g}$ condition. (c) Major axis length of Frank loops (green) and perfect loops (purple) as a function of damage level. Dash lines are fitting curves by power law with black lines representing linear growth of Frank loops in Ni ion irradiated by 650 keV electron beam at 693 K. [142] Figure adapted from He et al. [107]

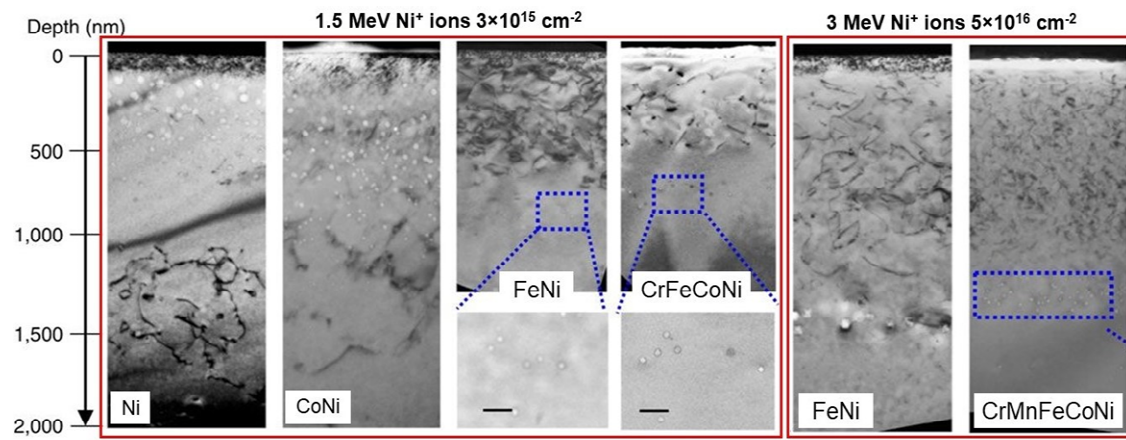


Figure A.12: Cross-sectional TEM images showing the distribution of dislocations, dislocation loops and voids in Ni, CoNi, FeNi, CrFeCoNi and CrMnFeCoNi irradiated with 1.5 or 3 MeV Ni ions at different fluences. Scale bar is 100 nm. Figure adapted from Lu et al. [23]

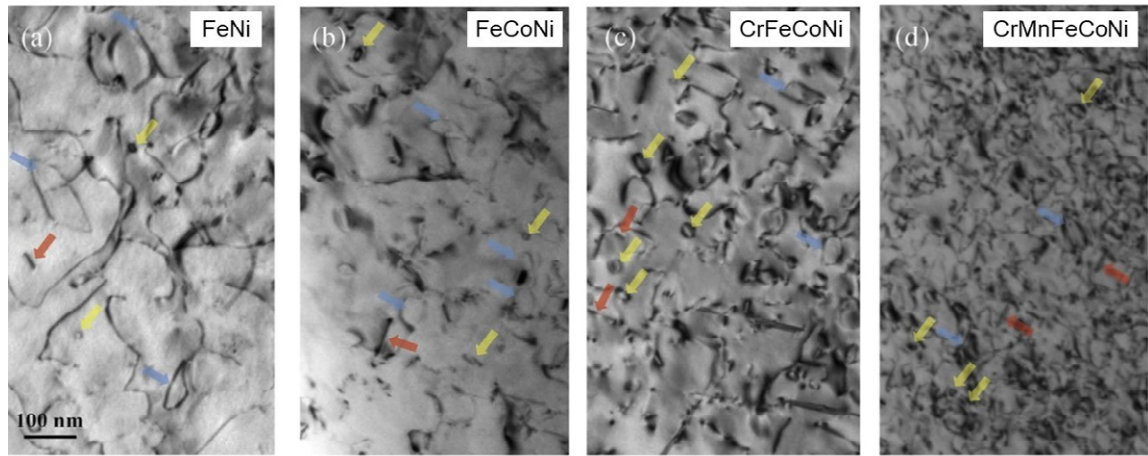


Figure A.13: Kinetic two-beam condition BF TEM images of dislocation loops in (a) FeNi, (b) FeCoNi, (c) CrFeCoNi and (d) CrMnFeCoNi irradiated with 3 MeV Ni ions at 773 K and up to 38 ± 5 dpa. Perfect, faulted and edge-on faulted loops are marked by blue, yellow and red arrows respectively [92].

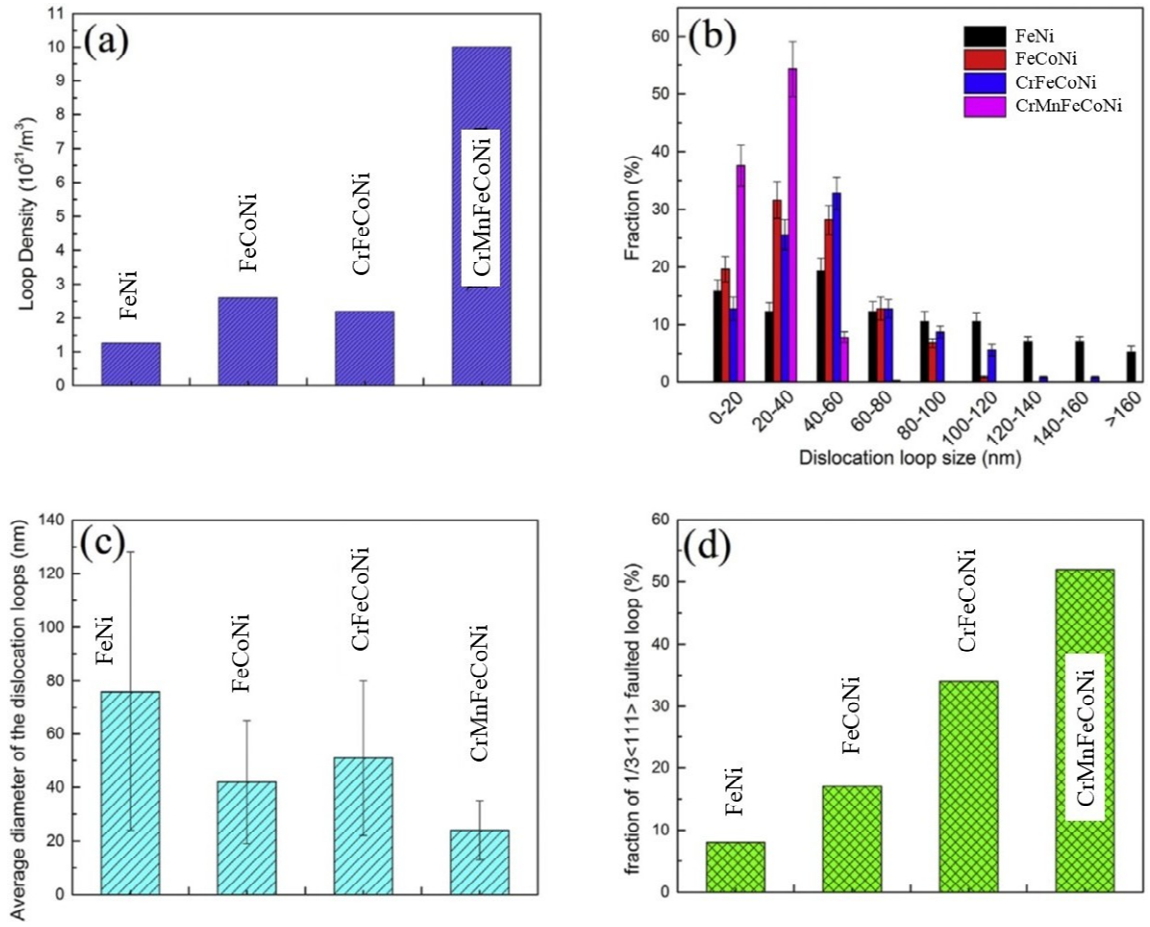


Figure A.14: (a) Loop density; (b) loop size distribution; (c) average diameter of loops and (d) fraction of $1/3\langle 111 \rangle$ faulted loops in FeNi, FeCoNi, CrFeCoNi and CrMnFeCoNi irradiated with 3 MeV Ni ions at 773 K and up to 38 ± 5 dpa [93].

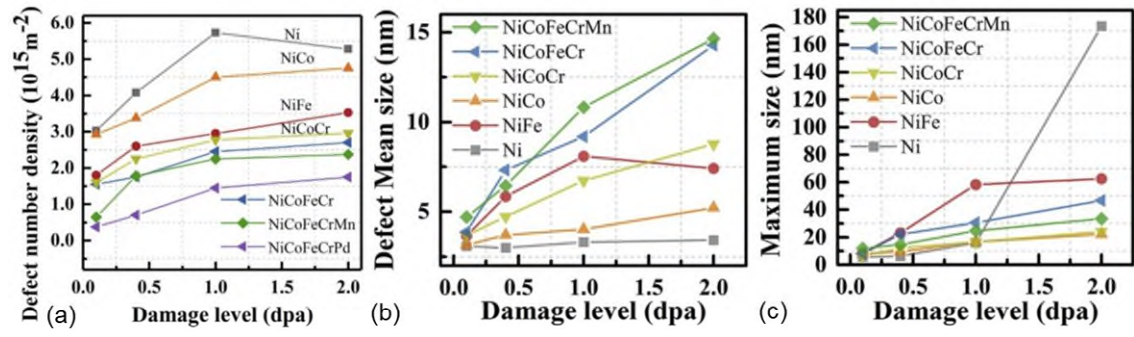


Figure A.15: (a) Defect density and (b) defect average size as a function of ion dose in Ni, FeNi, CoNi, CrCoNi, CrFeCoNi, CrMnFeCoNi and CrFeCoNiPd irradiated with 1 MeV Kr ions at a temperature of 773 K and from 0.1 to 2 dpa. Figure adapted from Shi et al. [114]

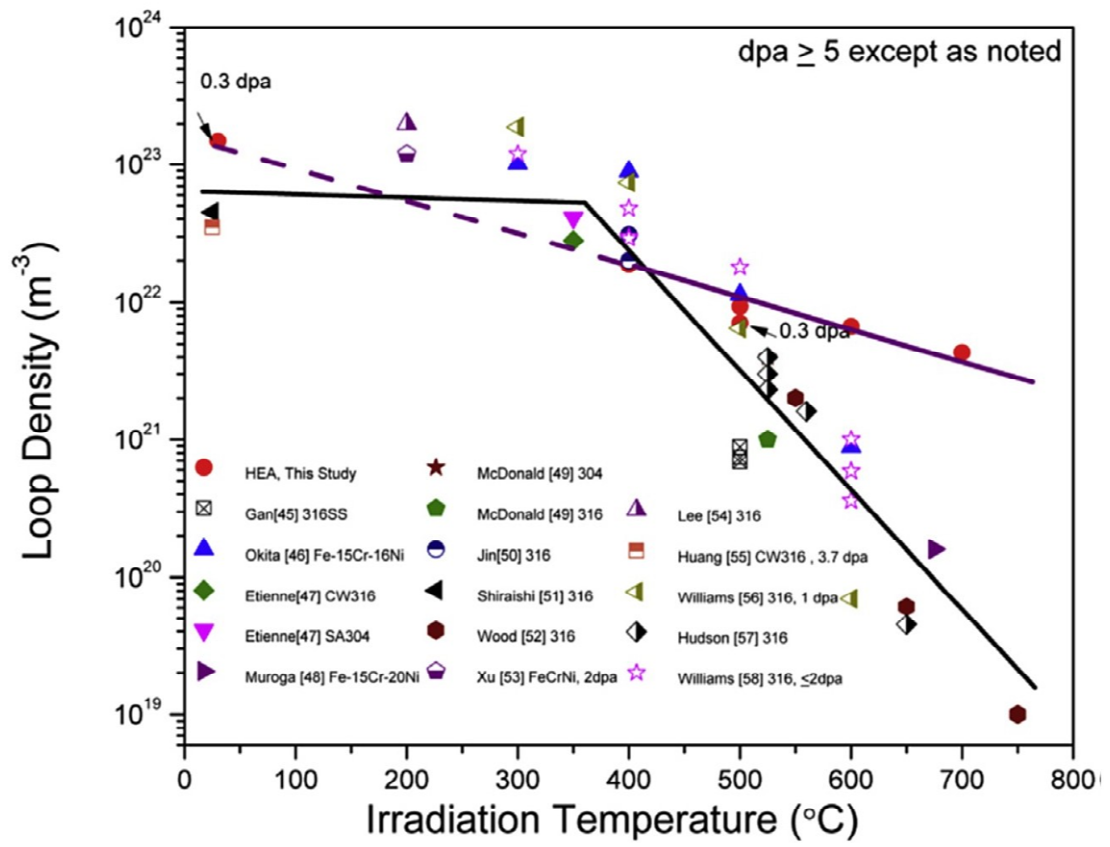


Figure A.16: Comparison of loop density versus irradiation temperature in $\text{Cr}_{18}\text{Mn}_{27}\text{Fe}_{27}\text{Ni}_{28}$ and conventional Fe-Cr-Ni austenitic alloys [115–128], irradiated at similar conditions [100].

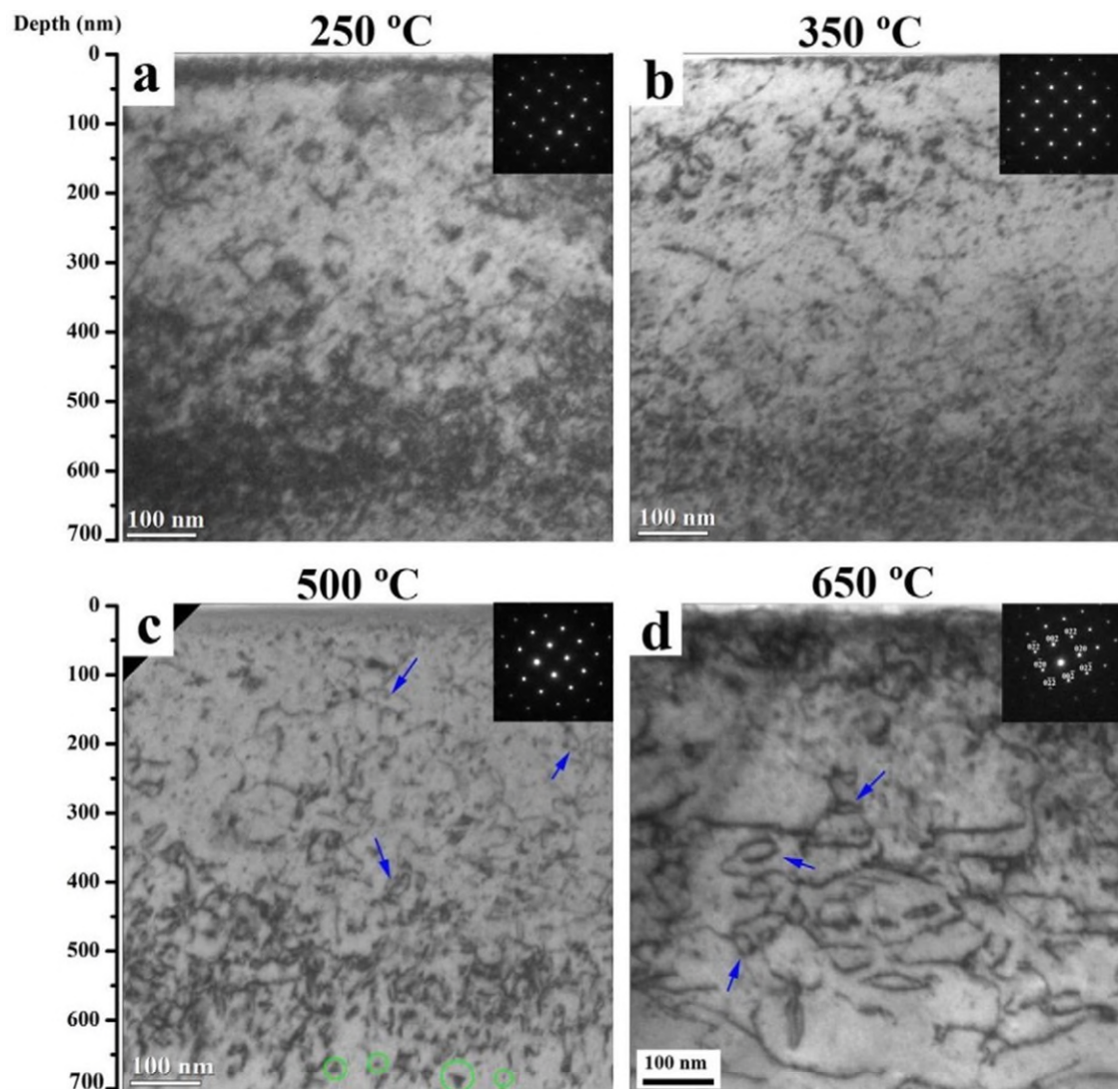


Figure A.17: BF TEM images and corresponding SAED patterns of a $\text{Al}_{0.1}\text{CrFeCoNi}$ irradiated with 3 MeV Au ions at different temperatures from 523 K to 923 K. Perfect loops and SFTs are marked by blue arrows and green circles [101]. Defect density decreased but defect size increased with increasing irradiation temperature.

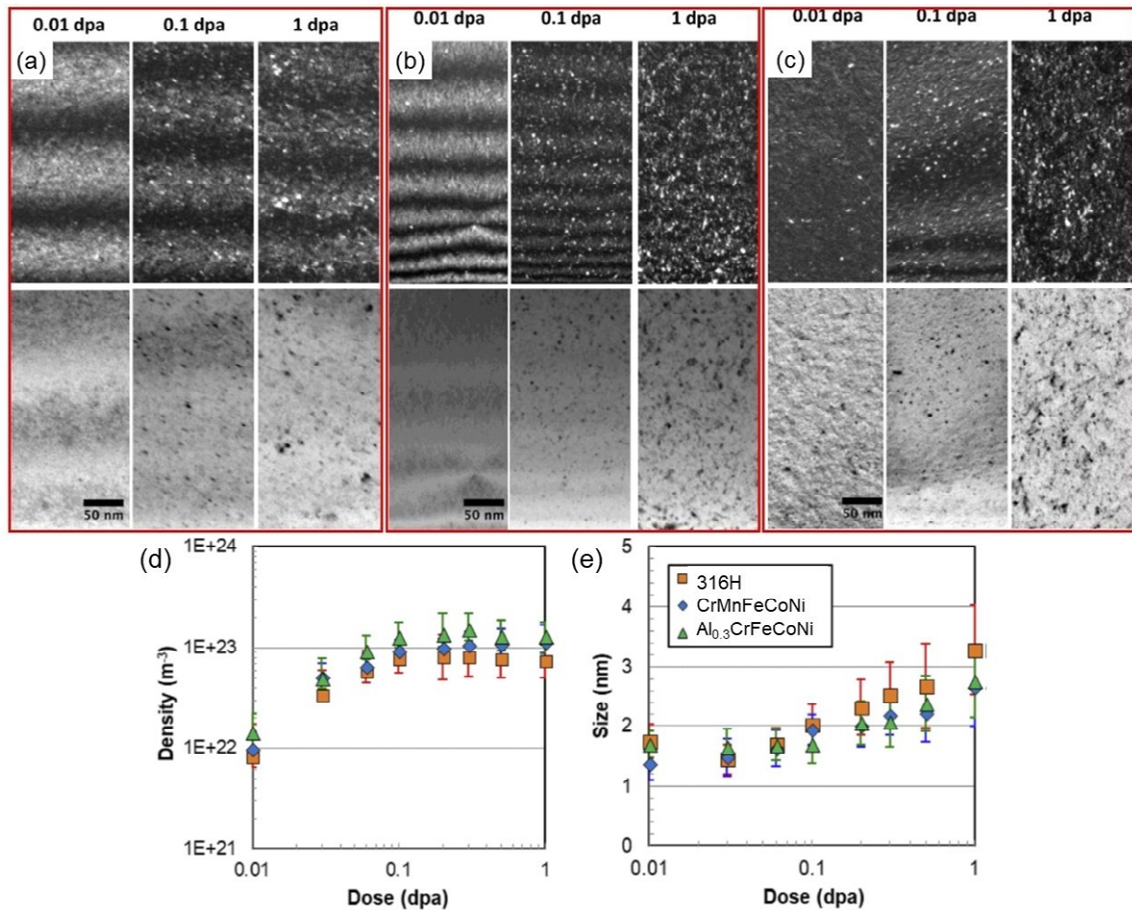


Figure A.18: WDBF (top) and BF (bottom) images of (a) 316H stainless steel, (b) CrMnFeCoNi and (c) Al_{0.3}CrFeCoNi irradiated with 1 MeV Kr ions at 573 K and different doses. (d) The loop density and (e) average size of loops as a function of dose in the three alloys respectively. Figure adapted from Chen et al [129].

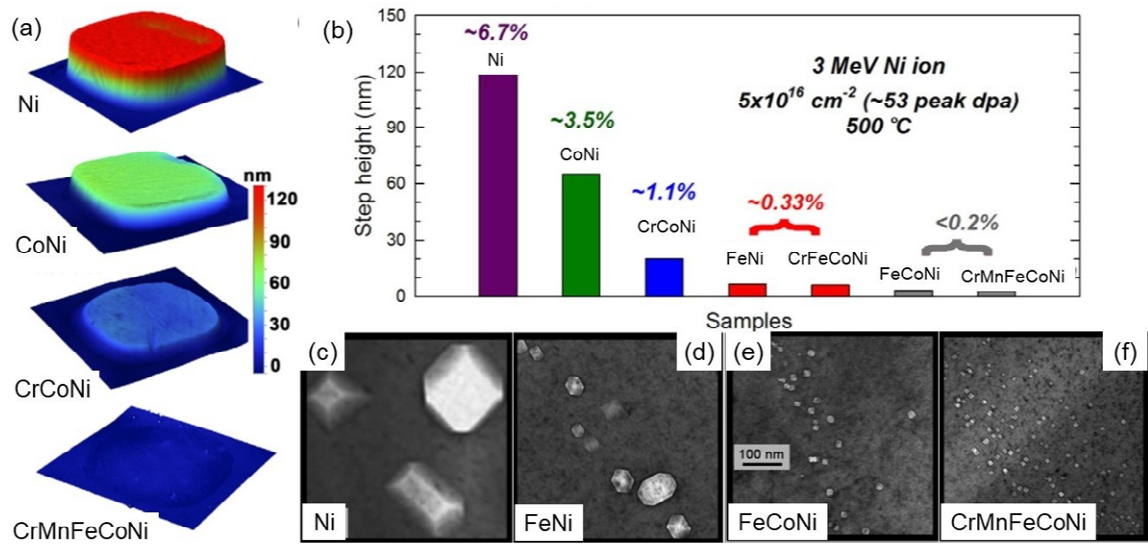


Figure A.19: (a) Optical profilometer measurements of void swelling in Ni, CoNi, CrCoNi and CrMnFeCoNi. (b) Step height change of each alloy after irradiation. Cross-sectional TEM images showing different sizes and density of voids in (c) Ni, (d) CoNi, (e) CrCoNi and (f) CrMnFeCoNi. Figure adapted from Jin et al. [133]

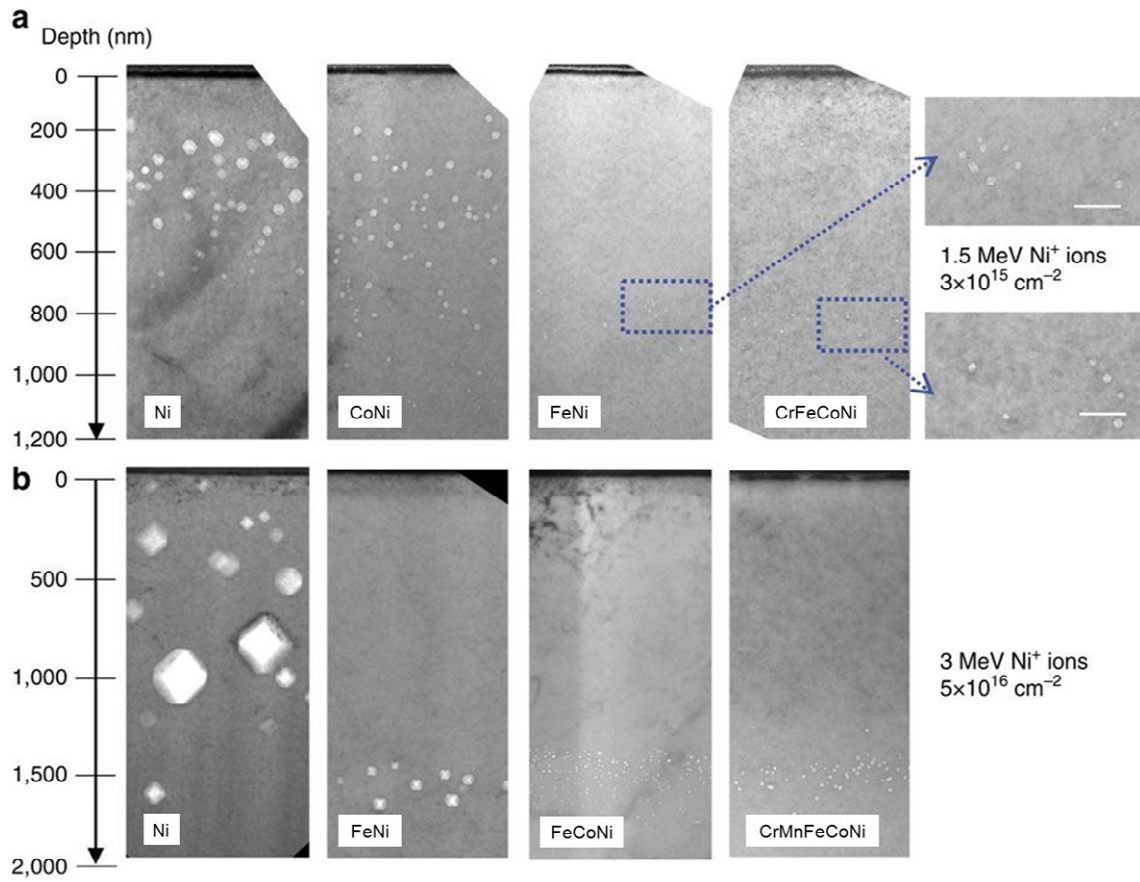


Figure A.20: (a) Cross-sectional TEM images of Ni, CoNi, FeNi and CrFeCoNi irradiated with 1.5 MeV Ni ions to $3 \times 10^{15} \text{ cm}^{-2}$ at 773 K with enlarged area marked by a dotted blue box; scale bar in the inset figures is 50 nm. (b) cross-sectional TEM images of Ni, FeNi, FeCoNi and CrMnFeCoNi irradiated with 3 MeV Ni ions to $5 \times 10^{16} \text{ cm}^{-2}$ at 773 K [23], showing reduced void formation with increasing compositional complexity.

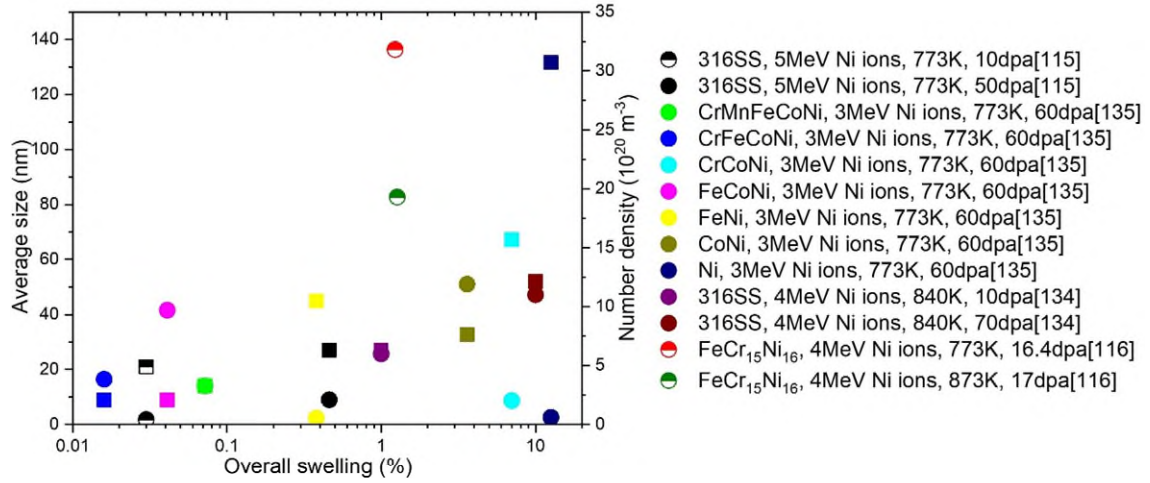


Figure A.21: The comparison of swelling behaviour between the Cantor alloy, its derivatives, and conventional steels (e.g. 316SS, FeCr₁₅Ni₁₆) under similar conditions [115,116,134,135]. Average size (nm, square marks) and the number density of voids (10^{20} m^{-3} , circles) are displayed as a function of overall swelling (%) in different materials. The irradiation conditions corresponding to each data point were included on the right where half hollow marks represented data obtained at the irradiation of ~10 dpa and solid marks represented data obtained at the irradiation of 50-70 dpa.

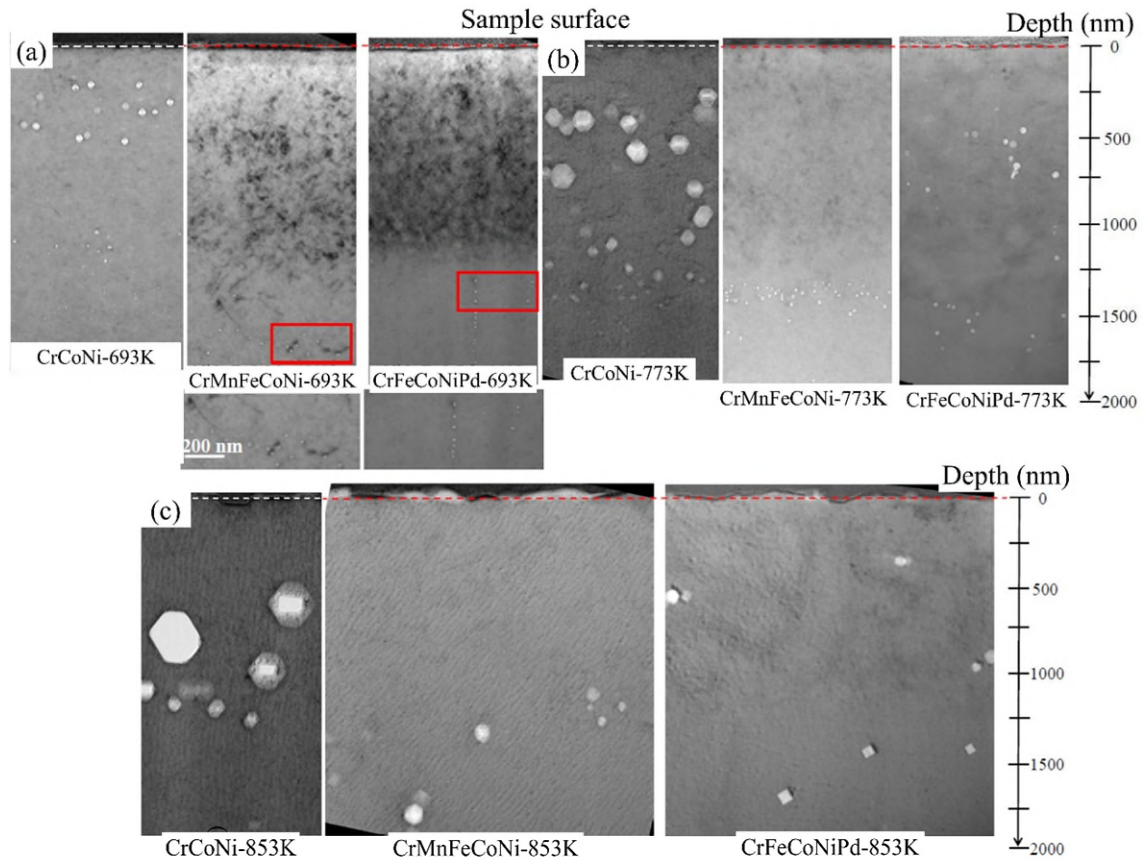


Figure A.22: Cross-sectional TEM images of CrCoNi, CrMnFeCoNi and CrFeCoNiPd irradiated with 3 MeV Ni ions at (a) 693 K, (b) 773 K and (c) 853 K, to a fluence of $5 \times 10^{16} \text{ cm}^{-2}$, showing dependence of void formation on composition and temperature. Figure adapted from Lu et al. and Yang et al. [92, 136]

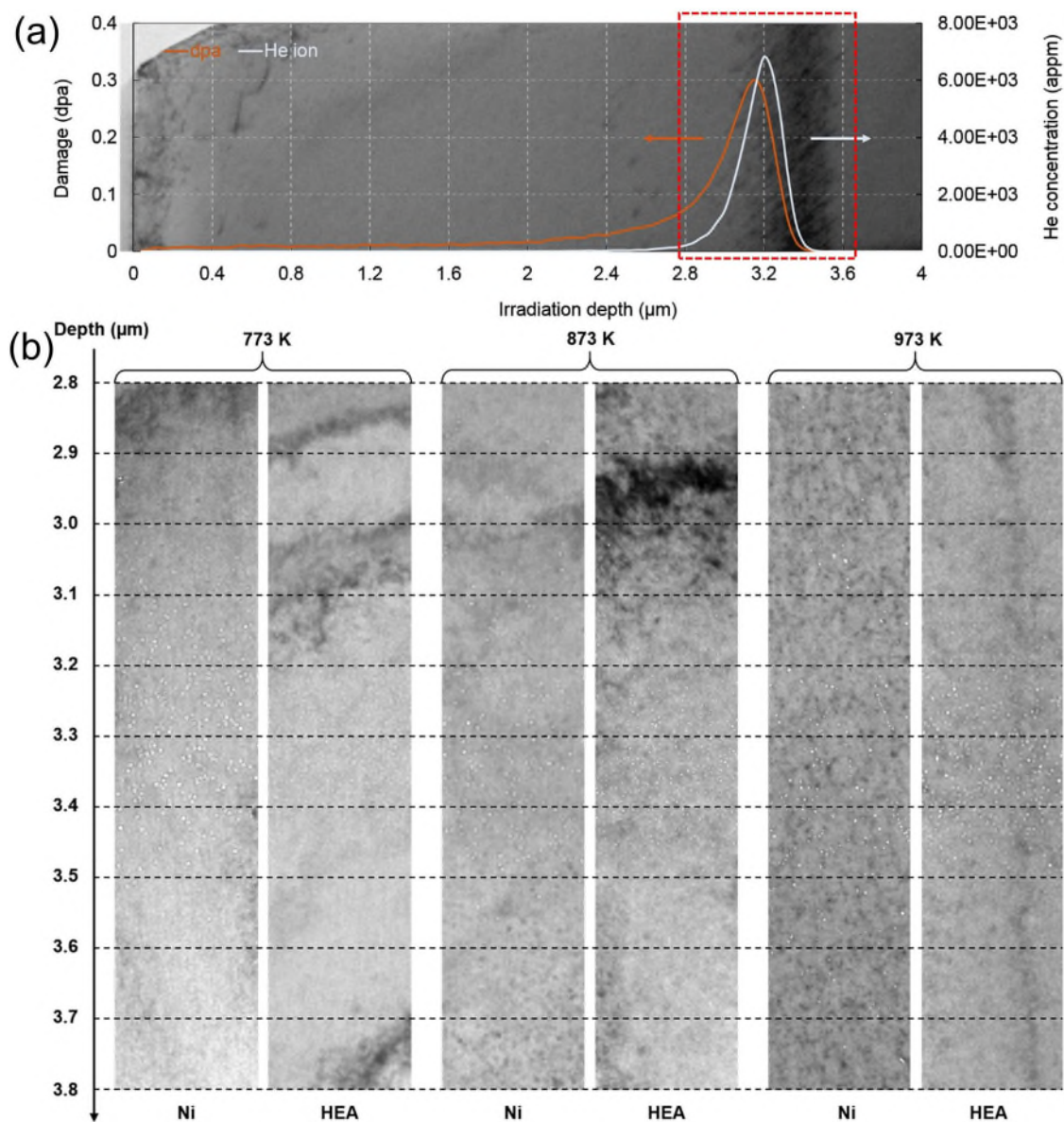


Figure A.23: (a) The Stopping and Range of Ions in Matter (SRIM) simulated ion radiation damage and incident He concentration profiles overlapped with a cross-section TEM image. The red dashed box indicates the peak damage region from where (b) was obtained. (b) Cross-sectional TEM images of Ni and CrFeCoNi irradiated by 2 MeV He ions at up to $1.52 \times 10^{16} \text{ cm}^{-2}$ fluence and (a) 773 K, (b) 873 K and (c) 973 K [141].

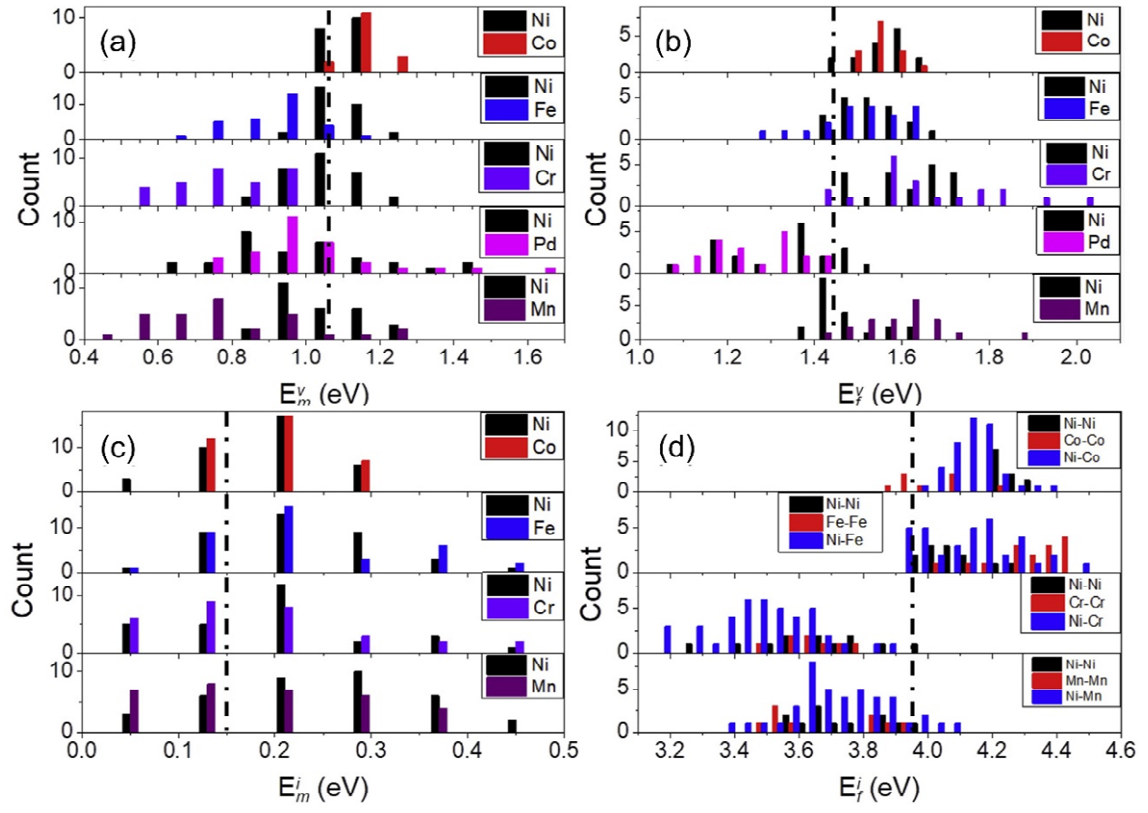


Figure A.24: (a) The migration (E_m^v) and (b) formation (E_f^v) energies of vacancies and (c) and (d) of interstitials (E_m^i and E_f^i) of $\text{Ni}_{80}\text{X}_{20}$ ($\text{X}=\text{Cr}, \text{Mn}, \text{Fe}, \text{Co}, \text{Ni}$ and Pd) binary alloys from DFT calculations. The dashed lines represent the energies in Ni. Figure adapted from Fan et al. [74]

List of Tables

- A.1 Summary of total void swelling in Ni, FeNi, FeCoNi, CrCoNi, CrFe-CoNi, CrMnFeCoNi and CrFeCoNiPd irradiated with 3 MeV Ni ions at 693 K, 773 K and 853 K. Data was from [23, 92, 135, 136, 143]. 69

Table A.1: Summary of total void swelling (%) in Ni, FeNi, FeCoNi, CrCoNi, CrFeCoNi, CrMnFeCoNi and CrFeCoNiPd irradiated with 3 MeV Ni ions at 693 K, 773 K and 853 K. Data was from [23, 92, 135, 136, 143].

T/K	Ni	FeNi	CrCoNi	CrFeCoNi	CrMnFeCoNi	CrFeCoNiPd
693	/	/	0.24%	/	0.02%	0.003%
773	9.4%	0.45%	7.01%	0.02%	0.07%	0.1%
853	/	/	9.34%	/	0.37%	0.3%